UCLouvain

epl

École polytechnique de Louvain

Towards a wearable impedimetric sensor for emotional sweat monitoring

Proof of concept

Author: **Anouk ROGIEST**
Supervisor: **Laurent FRANCIS**
Readers: **Benoit DELHAYE, Sébastien FANIEL, Denis FLANDRE, Laurent FRANCIS**
Academic year 2018–2019
Master [120] in Electro-mechanical Engineering

Acknowledgements

First of all, I would like to thank my supervisor Laurent Francis for his advices and great ideas. I would also like to thank Sébastien Faniel, Roselien Vercauteren and Grégoire Lebrun for their presence and their support during and outside meetings, as well as Denis Flandre for his precious sharing of knowledge.

To be able to machine a sensor like the one presented here, a lot of special skills, devices and materials are needed. I would therefore like to thank the entire Winfab UCL team, and especially Sébastien Faniel and Ester Tooten for their great know-how sharing and the time they have spent by my side using the different machines and devices. I would also like to thank Pascal Simon and Souley Djanjandi from the Welcome UCL team for their availability, their kindness and their precious advices.

I also address a special thanks to Isabelle Dargent for the patience, the kind availability and the understanding she provided me in various situations. My thanks also go to my co-worker Romain Hanus who helped me going through this thesis thanks to his support and generosity. A big Thank-you to my roommates who helped me to change my mind whenever I was feeling a bit lost or discouraged. And last but not least, I would like to thank my father for the incredible support and the review work on my paper, as well as the rest of my family and my friends for their presence and their support.

Abstract

Emotional sweat is used in electrodermal activity sensors in order to detect on-going epileptic seizures through the arousal of the sympathetic nervous system. Given that one third of the epileptic patients do not respond to drugs, the interest in such sensors has been growing due to their wearability, their non-invasiveness and their ability to monitor patient's skin over a long period of time. By scanning through an absorbent pad thanks to its interdigitated structure, the sensor herein developed captures additional parameters like conductivity and permittivity of sweat with the objective of enhancing seizure detection. The wearable sensor is designed to be flexible to properly fit the skin, and shall be positioned on the base of the thumb. Tests have shown a good discrimination between different salt concentrations, as well as a discrimination between different volumes of solution for de-ionized water. Thanks to promising results, this master thesis is the first step of a long journey towards a wearable impedimetric sensor product for emotional sweat and epilepsy detection and monitoring.

List of Abbreviations

SUDEP	Sudden Unexpected Death In Epilepsy
VNS	Vagus Nerve Stimulation
EEG	Electroencephalogram
ACM	Accelerometry
sEMG	Surface Electromyography
GTCS	Generalized Tonic-Clonic Seizures
EDA	Electrodermal Activity
IDE	Interdigitated Electrodes
PCB	Printed Circuit Board
DUT	Device Under Test
ALD	Atomic Layer Deposition
PDMS	Polydimethylsiloxane
PET	Polyethylene terephtalate
PI	Polyimide
EDL	Electrical Double Layer
AFM	Atomic Force Microscopy
WE	Working Electrode
CE	Counter Electrode
RE	Reference Electrode
DI	De-ionized water

List of Symbols

σ_{sol}	conductivity of solution
ε_{sol}	permittivity of solution
ε_0	vacuum permittivity
$\varepsilon_{r,sol}$	relative permittivity of solution
A_e	effective area
$W_s = d$	spacing between fingers
N_f	total number of fingers
R_{sol}	solution resistance
C_{sol}	solution capacitance
Z_{sol}	solution impedance
C_{ins}	insulating capacitance
c_k	cell constant
L_f	finger length
C_{dl}	electrical double layer capacitance
$f_z = \frac{1}{2\pi}\omega_z$	first cut-off frequency
$f_p = \frac{1}{2\pi}\omega_p$	second cut-off frequency
Z_{IDE}	equivalent impedance of the sensing unit
R_{ct}	charge-transfer resistance
θ_z	impedance phase
h_f	electrode height

Contents

Chapter 1

Introduction

Epilepsy is a well-known disease, which results in recurrent and sudden seizures. Due to temporary excessive neuronal discharges in the brain, the patient suffers from convulsions and/or altered consciousness. The seizures occurs randomly, which strongly affects the quality of everyday-life of the patient, and increases drastically the mortality ratios of affected patients. The need for caring solutions is stringent, since 65 million people suffer from epilepsy around the world, i.e almost 1% of the global population [1], [2], [3].

Thanks to the improvement of pharmaceutics, anti-epileptic drugs have been developed and allow 70% of patients to become seizure-free. Unfortunately, one third of patients continues to have seizures despite the drugs: this is what is called refractory epilepsy. For these people, reliable seizure detection is needed to allow an objective assessment of seizure frequency and therefore a tailored treatment to each individual patient. One step further, seizure prediction could tremendously increase the quality of life of patients since it would allow anticipation of seizures. Both seizure detection and seizure prediction could play a significant role in prevention of accident and of sudden unexpected death in epilepsy (SUDEP) [3], [4]. It can also help improving performances of techniques like vagus nerve stimulation.

Vagus nerve stimulation (VNS) is used since the 90s, and consists in scheduled stimulation, typically 30s every 5 minutes, of the vagus nerve through an implanted cuff electrode [5]. VNS was shown to have a great impact on epileptic patients when activated during ongoing seizure, as it shortens or abolishes the seizures. But even more, it has a cumulative effect: the frequency of seizures is decreasing for VNS-treated patients [6]. In this context particularly, seizure prediction would allow the initiation of stimulation before or at the onset of seizures, and would yet improve the efficiency of VNS.

Epilepsy, and particularly vagus nerve stimulation, are the driving forces behind this master thesis. More precisely, the thesis consists in researches for a monitorable biological signal to be coupled with information collected thanks to a cuff electrode placed on the vagus nerve when practicing VNS. By merging both signals, a

more reliable/earlier seizure detection is expected, which will hopefully lead to an improvement in VNS outcome. Affected patients would thus get a better control of their disease, and therefore a better quality of life.
The used biological signal has to be continuously monitored, since it is the only way to detect every occurence of seizure. In continuous monitoring research area, wearable non-invasive sensors become really attractive, since their set-up is easier, lighter, more comfortable and less exposed to infections [7]. Electrodermal activity is one of the ways to noninvasively detect seizures, using the arousal of the sympathetic system through activation of a certain kind of sweat glands located on glabrous skin [8]. For now, electrodermal activity is monitored by detecting changes in skin conductance. The question behind this thesis was then to see if some additional information related to seizures could be extracted from the same sweat glands. Following this purpose, the choice was made to create an impedimetric interdigitated sensor for monitoring the secretion of these sweat glands. Hope is to observe some new perspectives of seizure detection through sweat characterization.

This thesis will thereby focus on a proof-of-concept of a flexible, wearable interdigitated sensor for monitoring perspiration on the palm of the hand, where the sweat glands are located. The next section explain the reasoning which led to the decision of designing a perspiration sensor, followed by a complete state-of-the-art on sweat sensors. Afterwards, one chapter speaks about the design and fabrication processes while the other presents experimental validation of the sensor. Conclusions are then drawn, after suggesting some key areas for further research and development.

1.1 Research context

1.1.1 Epilepsy complexity

Epilepsy is a very complex disease to handle, because it has many different sources, many ways of showing up and plenty of patient-specific parameters. For now, seizure tracking is handled by the patient and family members or by healthcare personal, but it is strongly influenced by the level of awareness of seizures and by sleep [1]. According to studies, EEG is recording 29 times more seizures than family members, and 7 times more seizures than doctors. However, only a reliable and precise seizure quantification can lead to a tailored treatment. This is why several seizure detection devices based on biological signals have emerged, as exposed in the list below [3]:

- Electroencephalogram (EEG)
- Intracranial EEG
- Surface electromyography (sEMG)
- Electrodermal activity (EDA)
- Electrocardiography (ECG, EKG)
- Accelerometry (ACM)
- Video detection systems
- Mattress sensors
- Seizure-alert dogs
- Implanted advisory systems
- Cerebral oxygen saturation sensors
- Near infrared spectroscopy (NIRS)
- Skin temperature
- Respiratory monitor

Unfortunately, none of these devices is able to detect every kind of epileptic seizures. There are about a dozen different seizure types; the main ones are GTCS (generalized tonic-clonic seizures), myoclonic, tonic, clonic, hypermotor and autonomic seizures. Each of these seizure type consists in one or more phenomena occuring simultaneoulsy or sequentially, including body motion, physiological changes and/or altered consciousness.

Some sensors are used for motion detection (ACM, sEMG, video monitoring, mattress sensors, etc.) while some others detect changes in biological signals like heart rate, respiratory rate, sweating and temperature [3]. For every type of seizures, hope is to find a combination of sensors to maximize the seizure qualification and quantification [1]. But this is more complicated than it seems, because seizures also vary within the same type, depending on the patient. Seizure detection devices are then to be designed for each and every patient depending of his seizure demonstration.

EEG is the gold standard for seizure detection in hospital, but it requires a nursing staff and is not wearable outside the building [1],[2]. Therefore, despite the good sensitivity and detection threshold given by this device, the common interest shifts to devices allowing easy point-of-care testing. One of the major challenges of seizure detection devices is indeed to allow the patient to live his/her every-day life with control on his/her disease, in order to tremendously improve the quality of life. The wearable and non-invasive sensors thus become very attractive, since the setup is easier, more comfortable and less exposed to infections.

Following a private interview with Prof. Riem El Tahry, neurologist at UCLouvain, we learned that her research purpose is to increase VNS outcome. VNS is done using a cuff electrode on the vagus nerve, and can thus easily record information from this nerve. Since the vagus nerve plays an important role in cardiac and respiratory regulation, the cuff electrode gives access to these signals. Nevertheless, the cardiac information is more used than the respiratory ones, because heart rate is only regulated by autonomic system, while breathing can be influenced by voluntary control (apnea, effort, etc). The vagus nerve is also part of the sympathetic system, which is generally activated to prepare the human body to face stress and fight-or-flight situations.

To create reliable multi-modal seizure detection and/or prediction, a relevant biological signal need to be monitored and coupled with vagus nerve related information. The search for this signal is therefore a central task to realize. As it is just mentioned, wearable non-invasive sensors show better capability for long-term continuous monitoring. There are two different kinds of wearable and non-invasive sensors, and the ones monitoring physiological signals are preferred over motion detection sensors because of their higher likelihood to early seizure detection.

Electrodermal activity (EDA) record a physiological signal, and was selected over skin temperature sensors or cerebral oxygen saturation sensors because of its feasibility, easy data extraction ability and already known efficiency. EDA reflects the activation of the sympathetic nervous system through eccrine sweat glands, and is therefore a parameter quite often used in seizure detection [8], [7]. The next section further explains the sympathetic system and the role of EDA in seizure detection.

1.1.2 Epidermal activity and sympathetic system

In epilespsy, there is a recurrent interest in autonomic variables, because many seizure types involve autonomic dysfunctions. Wearable sensors detecting autonomic variables are therefore an interesting way to get a reliable seizure detection, instead of EEG or iEEG [7], [9].

So far, the most used signals for autonomic alterations are heart rate, respiratory rate and blood pressure, which are all regulated by both parasympathetic and sympathetic systems. Electrodermal activity is an exception, as it only depends on sympathetic activity. There are indeed sympathetic post-ganglionic fibers surrounding eccrine sweat glands and modulating sweat secretion. Therefore, the change in skin conductance, named electrodermal activity, is the only parameter reflecting purely sympathetic activity [8].

Links between EDA and epilepsy have already been observed more than once. According to (P. Rylvin et al, 2018 [10]), EDA has shown large increases and long post-ictal [1] elevation of conductance level after spontaneous seizures, mostly in GTCS. SUDEP is strongly assosiated with GTCS, which make GTCS one of the seizure types where the need for reliable seizure detection is really stringent. (M.-Z. Poh et al, 2010 [8]) also predict that the periods of post-ictal EDA elevation could be linked to impaired vagal reactivation, leading EDA to be a sign in SUDEP pathology.

More generally, electrodermal activity and/or heart rate have shown significantly different values between interictal [2] and preictal [3] states, in several types of seizures. EDA is thus a promising tool for seizure detection regardless of the seizure type. Another great advantage of EDA is that it is non-invasive, which leads to easier continuous monitoring.[7]

1.1.2.1 Anatomy behind electrodermal activity

Electrodermal activity is the term used for changes in skin conductance, especially phasic changes named *galvanic skin responses*, which are the consequences of sympathetic arousal. The slow shifts in skin conductance level (SCL) and the more transient skin conductance responses (SCR) are both qualified as galvanic

[1] as ictal is an adjective related to an ongoing seizure, post-ictal means that it occurs after a seizure

[2] between seizures

[3] before seizure onset

skin responses [11].

EDA is measurable on the glabrous skin; the palms of the hand or the soles of the foot, thanks to eccrine sweat glands activation. Eccrine sweat glands are coiled, tubular structures going from epidermis to lower dermis, as represented on figure 1.1. They are found over the whole skin, but the largest concentration of eccrine sweat glands is on the glabrous skin, about $400/mm^2$ [11]. The outer diameter of the secretory coil is $30 - 60\mu m$, and its depth is around $2 - 4mm$ [12]. Unlike apocrine sweat glands which secretes into hair follicles, eccrine sweat glands secretes directly at the skin surface (see Figure 1.2).

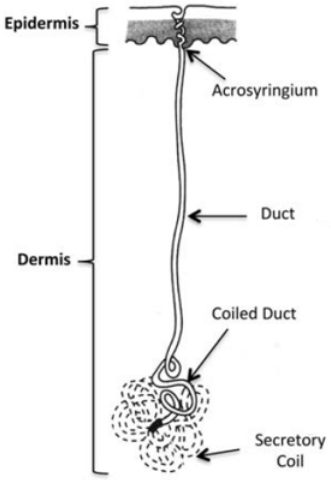

Figure 1.1: Anatomy of a single eccrine sweat gland [12]

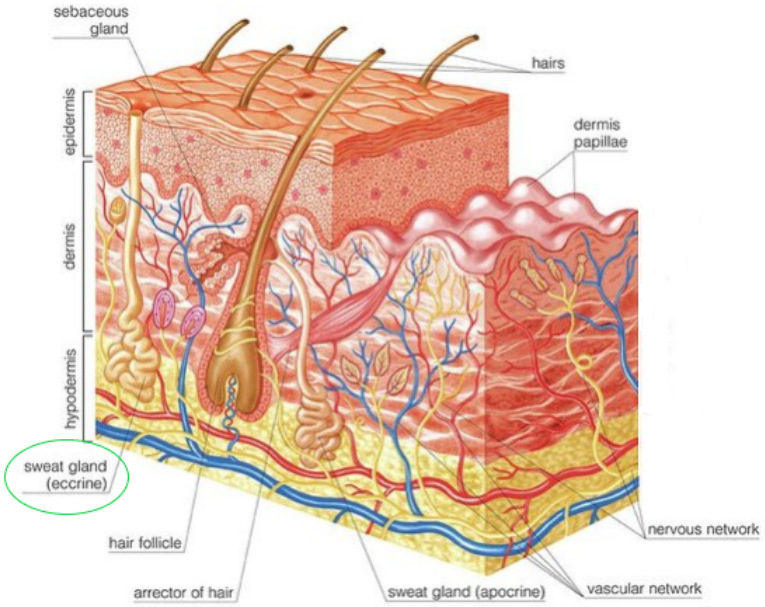

Figure 1.2: Eccrine sweat gland environment [13]

Sudation mechanism working principle [12] The mechanism behind sweat secretion is really complex and not completely understood, but a simplified and broad explanation is enough in this context. The Figure 1.3 just below explains the summarized sudation mechanism.

Cl^- ions accumulate in cells around the coil lumen against an electrochemical gradient thanks to a mechanism involving Na^+ transporters, K^+ channels and Na^+/K^+ pumps. When Ca^{2+} cations arrive from nervous influx, it open Ca^{2+}-activated Cl^- ions channels. Cl^- ions then diffuse fast into gland lumen. Thanks to electrochemical gradient caused by Cl^-, Na^+ cations pass paracellularly into the lumen to join Cl^- anions. Na^+ and Cl^- bonds and forms NaCl, which creates an osmotic gradient for water to pass into the lumen.

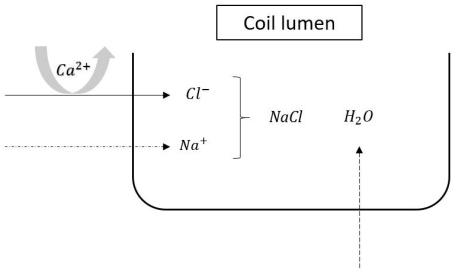

Figure 1.3: simplified sudation mechanism

This first fluid in secretory coil (figure 1.1) is isotonic to plasma, meaning that it has the same concentration of solutes than plasma ($[Na^+] \approx 145 mmol/L$, $[Cl^-] \approx 115 mmol/L$). However, at the skin surface, solutes concentration are lower ($[Na^+] \approx 70 mmol/L$, $[Cl^-] \approx 80 mmol/L$), because there is a solute reabsorption in the duct. The fluid at skin surface is therefore hypotonic to plasma.
When the sweating rates increase, there is less time for the solutes to be reabsorbed in ducts, and the salt concentration in sweat is therefore higher. Salt concentration in sweat in thus a good indicator of sweat rates.

Eccrine sweat glands on hairy skin play a role in thermoregulation, but those on the glabrous skin reflects sympathetic activity, since there are innervated by sympathetic post-glanglionic fibres. The sympathetic nervous system is strongly related to emotion, since it's the one in charge of handling danger and stressful situations. EDA is therefore a psycho-physiological index for *emotional sweating* [14]. Sweating on the palms and soles allows humans, as well as monkeys, to get a better grip for rapid escape or precise manipulation. Eccrine sweat glands can thus be activated by deep respiration, mental stress or local tactile stimulation.

However, sweating on palms and soles is not always associated with emotional events: physical exercise, local stimulation and thermoregulation also influence the sweat level. Despite this, a way to separate emotional sweat from thermoregulation exists. Thermoregulation is indeed slow-adaptive, while a stimuli coming from sympathetic system will generate a quick increase in sweat level, which then rapidly returns to baseline. It is thus possible to observe and discriminate both behaviours on the same graph [14].

1.1.3 Sensor development

The secretion of eccrine sweat glands is a sterile, dilute electrolyte solution mainly composed of potassium, bicarbonate and NaCl. As EDA only relies on conductance changes, the goal is to get more information about emotional sweat, hoping to be able to link them with seizure arousal. Two attractive variables to be analysed are the NaCl concentration and sweat level.

1.1.3.1 Challenges of skin scanning

The first idea for the sensor design was to scan the skin with 2 different depths, in order to visualize the behaviour of sweat both in the secretory coil situated in the lower dermis, and in epidermis. It could have allowed us to get some pattern in the sudation mechanism linked with sympathetic system activation in epileptic seizures.

There are indeed some unresolved questions concerning the sweat mechanism. One of them is that even though we perfectly know that the sweat output increases in response to heat or exercise, it's not clear whether it is the cellular mechanisms acting faster, or an increase in mechanism components that allows this increased output.[12] As there are some grey zones in chemical working principle, the hope using skin impedance analysis is to observe some kind of electrical pattern when eccrine sweat glands are activated during epileptic seizures. Another advantage in impedance sensing is the ability to extract parameters such as conductivity and permittivity, which give information about sweat nature.

To execute this idea, an encapsulated interdigitated (IDE) sensor was chosen. The use of the fringing field effect between two electrodes would indeed allow us to scan the skin with different depths, depending on the spacing between electrode fingers. The sensor would have been in direct contact with skin, and the electrical field lines would have scanned into the skin. Such sensor implementation faces a lot of challenges, listed just below.

1. Mean values for dermis and epidermis depths on palms can be found, but the location of secretory coils are actually quite patient-specific. As we know, there are located in the lower dermis. The first issue is that the skin shrinks with age, which affects the secretory coil depth. The second and most important issue is the cornified layer. This layer, called stratum corneum, is the most superficial layer in skin, and is mostly composed of dead cells. Depending on the patient activities, stratum corneum can grow up to 5mm, causing the IDE to be completely irrelevant.

2. Dermis contains plenty of components like blood vessels, nerves, hair follicles, etc.(see figure 1.2) and secretory coils are not bigger than $60\mu m$, meaning that all these components are found next to each other [12]. As the primary sweat produced in secretory coils is isotonic to plasma, which is the main component of blood, there will be no way to distinguish the sweat gland activity from the blood vessel activity.

3. The skin has a dielectric constant which depends on a variety of parameters. Due to all the regulation mechanisms happening within skin (vasoconstriction/vasodilatation, inflammatory soup, etc.), it might be really difficult to somehow link the impedance measurement with a concrete perspiration data.

4. When the sensor is placed directly on skin, there is no way to evacuate the sweat at the surface. It will then accumulate at the sensor-skin interface, create an easier electrical path for the field lines to pass through, and therefore influence the measurement.

Since all these challenges would have caused errors and irrelevance in the measurement, an easier and more reliable sensor implementation was selected, presented in section 1.1.3.2.

1.1.3.2 Substrate scanning implementation

Looking at the state-of-the-art in section 1.2.2 concerning interdigitated sweat sensors, most of them are not scanning into the skin, but rather scan a porous material placed between the sensor and the skin. The benefit of using an absorbent pad is that it has a known dielectric constant, and therefore the sensed changes in capacitance will be directly related to presence of sweat into the dielectric.
The absorbent pad will attract water by capillarity, thus requiring no driving force for sweat collection. It will also allow easier evaporation of sweat than direct skin contact, and avoid skin irritation that can exist due to friction with solid materials.

This kind of sensor could allow easy characterization of emotional sweat by extracting sweat permittivity and conductivity out of the sensed impedance. The state-of-the-art in next section thus focuses on wearable, flexible sweat sensors with an increased interest into substrate scanning sensors. The following sections discuss the design, materials and fabrication methods needed in order to create such a device. An experimental validation of the created sensor is done in the subsequent section, in order to prove the feasibility and the proper functioning of the sensor, with respect to its environment, i.e. the skin.

1.2 State of the art

1.2.1 EDA electrochemical sensors

Electrodermal activity is based on the principle that skin resistance (or skin conductance) vary with the state of sweat glands in the skin [8],[7],[15]. Nowadays, these variations in sweat gland activity are measured with 2 electrodes placed on the palmar surface of hand, mostly on medial or distal phalanges,as on Figure 1.4. A small DC current is applied to stratum corneum beneath the measuring electrodes, and therefore the changes in sweat gland activity are sensed as changes in electrical conductance.
The electrodes are made of Ag/AgCl, which role is to converse the ion current at the surface of skin into electron current.

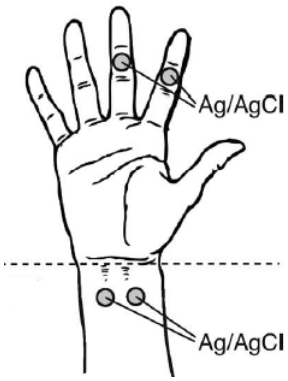

Figure 1.4: electrode attachment sites [15]

As said before, the preferred sites for the electrodes are on the palmar side of the hands to find glabrous skin. However, several studies have shown that ventral side of distal forearm (see bottom part of 1.4) is a viable alternative for EDA measurements. With this location, the measurement is less exposed to motion and pressure artefacts.

1.2.2 Wearable sweat sensors

As the goal of this thesis is to create an interdigitated sensor in order to assess whether it can bring some new perspectives in eccrine sweat analysis, the state-of-the-art herein focuses on wearable, flexible interdigitated perspiration sensors.

Sweat characterization has much larger range of application than just sensing the arousal of sympathetic nervous system. Depending on the location and technology, wearable sweat sensors can monitor health and wellness, physical performances, hydration level, salt losses and they can even help with diagnosis of diseases like diabete.

Both [16] and [17] use sensitive electrodes for electrochemical sensing of several parameters, i.e. Cl^- ions, glucose, pH in sweat, using the same principle as explained in section 1.2.1. Changes in conductances can also be sensed using other detecting principles like in [18], where the changes are observed between two wires, or in [19], where there are sensed thanks to a R-C parallel dipole on a PCB.

All the others sensors use interdigitated electrodes technology for sensing either conductivity changes, skin hydration level or other chemical properties of sweat, through impedance analysis.

We can differentiate [17], [20], [21], [22], [19] from [16], [18], [23], [24] because the first ones are strechable while the other ones are flexible sensors. This flexible/strechable characteristic is needed to properly fit the skin, and stay close to it whenever the skin is streched or folded because of body movements. The general case is that PDMS is used as strechable substrate while polyimide film is used for flexibles ones. However in [22], polyimide is used for a strechable sensor because the electrodes fingers are not deposited on a substrate like all the others, they are rather fully encapsulated, finger by finger. That method strongly reduces the impact of polyimide high tensile modulus.
Both PDMS and polyimide are selected over a wide range of polymers because of their inertness and biocompatibility.

Concerning the electrodes, it appears that whenever the sensor is strechable, the predominant choice is to use serpentine-shaped interdigitated electrodes, because it provides flexibility and strechability to the sensor while maintaining its functionality under dynamic body movements. The electrode material is either gold, aluminium, copper or nanowires, with a higher tendency for gold. The three metals are biocompatible, but gold is a noble metal, which makes it withstanding both oxydation and corrosion. With regard to nanowires, they are more flexible conductive materials than pure metals.

In the list of sensors mentionned in Table 1.1, only [20] is scanning directly onto the skin. Otherwise, all the IDE sensors scan into an absorbing pad. Whenever the pad material is described, it turns out to be cellulose. The absorbent paper attracts sweat by capillary action, and no other driving force is needed. Instead of

an absorbent pad, in [19], hydraulic pumping is done by creating tubes into PDMS, so that the sweat is driven at the circuit PCB surface.

To fix the sensor on skin, either sticky Silbione®silicones [17], spray-on bandages [21] or a Tegaderm™backing layer [18], [22], [23] are used. They all are certified medical equipments used to hold devices (perfusion needles, sensors) close to skin.

Summary	Application	Date	Flexible/ Strechable	Electrodes	Substrate	Illustrations and References
electrochemical sensing of Cl-	hydration state and salt loss	2015	flexible	RE + chloride sensitive (AgCl) electrodes	PET substrate + gauze for sweat collection	Figure A.1, Reference [16]
electrochemical sensing of glucose and pH in sweat	heath management and diabete diagnosis	2018	strechable	RE, pH and glucose (AuNS) sensing electrodes.	strechable substrate + sticky silbione for attachement to skin	Figure A.2, Reference [17]
IDE sensing of conductivity changes due to Na+ and Cl- concentration	wellness monitoring and performance analysis	2017	stiff	serpentine-shaped Al interdigitated electrodes	glass wafer substrate + absorbant paper	Figure A.3, Reference [25]
IDE sensing skin hydration level by change of impedance due to increased dielectric constant	continuous monitoring of skin hydration and other health parameters	2017	strechable	silver nanowires interdigitated electrodes	PDMS substrate placed on skin	Figure A.4, Reference [20]
sensing of increased conductance on armpits	Continuous recording of sweat excretion	2018	flexible	copper-based electrodes	Kapton film with apertures for evaporation + absorbing pad. Fixed on skin with Tegaderm™	Figure A.5, Reference [18]
LC resonators with capacitive electrodes for volume and chemical properties of sweat	epidermal analysis of biofluids	2014	strechable	serpentine-shaped (Au) for electrodes	electrodes encapsulation with polymide, placed on PDMS + substrate for sweat collection. Spray-on bandage as adhesive leads	Figure A.6, Reference [21]
IDE sensing of skin hydration level through RC measurements	continuous sweat monitoring	2012	strechable	serpentine-shaped (Au) for electrodes	electrodes encapsulation with polymide + adhesive backing layer Tegaderm™+ cellulose pad	FigureA.7, Reference [22]
sensing of conductivity changes with RC parallel dipole	physiological condition monitoring	2016	strechable	R//C on PCB for conductivity sensor	hydraulic pumping by tubing in PDMS	Figure A.8, Reference [19]
IDE sensing of sweat rate and level through capacitance	sport performance, dehydration monitoring, and health assessment	2013	flexible	interdigitated (Cu) electrodes	Kapton film substrate + cellulose pad fixed with scotch tape and loctite 4011 epoxy + Tegaderm™for skin adhesion	Figure A.9, Reference [23]
capacitive coupling through insulating layer	capacitive sensing of electrophysiological signals	2013	flexible	measurement, ground and ref (Au) electrodes	electrodes insulated in silicone	Figure A.10, Reference [24]

Table 1.1: State-of-the-art of wearable sweat sensors

Chapter 2

Sensor design and fabrication

The electrical response in stimulation of a liquid consists in a R-C parallel dipole because of its finite conductivity and permittivity. Therefore, impedance analysis is used to extract both liquid conductivity σ_{sol} and permittivity ε_{sol} out of the resistive and the capacitive components, respectively. Motivation to measure these parameters is to collect useful information for fluid identification.

2.1 Sensor design

2.1.1 Sensor implementation

The purpose of the sensor is to sense the emotional sweat coming out of eccrine glands when the sympathetic system is activated during epileptic seizures. As explained in section 1.1.2.1, these glands are found on the glabrous skin, that is the palms of the hands or the soles of the feet. The decision was made to wear the sensor on the palms of the hands. On the foot, measurements would have been indeed too much influenced by motion artefacts and by humidity due to perspiration in a closed environment: shoes.

The sensor location was chosen in order to miminize skin motion artefacts. After observation, it seems that the base of the thumb (see Figure 2.1a, 2.1b) is one part where skin does not fold too much, and moreover, is not really used for manipulation as often as distal and medial phalanges.

(a) Sensing unit location

(b) Sensor placed on skin

About sensing unit, the global scheme is presented in Figure 2.2. Gold electrodes

are deposited on polyimide film, and then insulated with Al_2O_3 deposition using ALD (Atomic Layer Deposition). Spacing between electrode fingers is made so that it allows a scan within the pad thickness. The sensor unit is flipped in order to have the insulating layer facing the absorbent pad, which is in contact with skin.

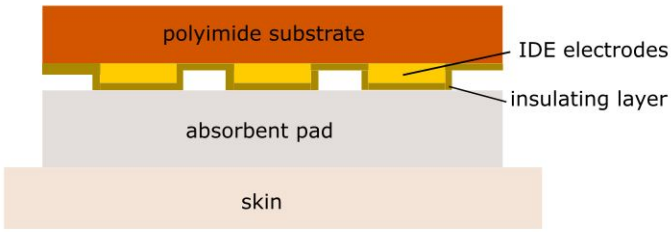

Figure 2.2: Cross-sectional view of sensor design (not on scale)

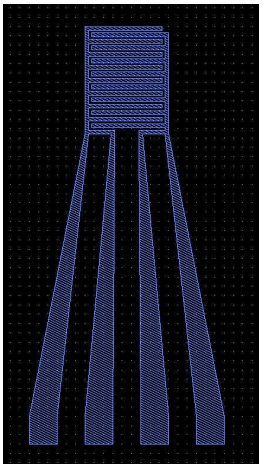

Figure 2.3: Top view of sensor design (Layout Editor)

As the sensor will be scanning the base of the thumb, connectics include routes encased in polyimide which turn aroung the thumb to reach the dorsal side of the hand, where the accesses will be much easier. These routes have an increasing width while going towards to connecting pads, in order to reduce parasitic lead resistance (see Figure 2.3).

Our sensor is designed to be flexible, in order to get a smart fitting of the skin. Using flexibility over stretchability allows an easier implementation of the interdigitated structure, since it therefore does not require serpentine-shaped electrodes. The cellulose pad also represent a challenge to create a stretchable sensor, while it is easy to use in a flexible sensor.
x

2.1.2 Impedance analysis: Four-terminal sensing

Four-terminal sensing is an electrical impedance measuring technique that allows more accurate measurements than usual 2 points sensing. It consists of 2 separate pairs of electrodes, one pair called current-carrying and the other called voltage-sensing electrodes.

The current-carrying electrodes (force connections, number [1] and [2]) leads

current I_m through the device. Using traditional 2-point sensing with only this pair of electrodes, the voltage drop around the device under test (DUT) would have been measured using Ohm's law $V = RI$. Unfortunately, the sensed resistance in this case would include R_{DUT}, but also the contact resistance and the lead resistance, represented as R_{par} on the Figure 2.4 below. The sensed voltage drop would have been greater than the actual V_{DUT}.

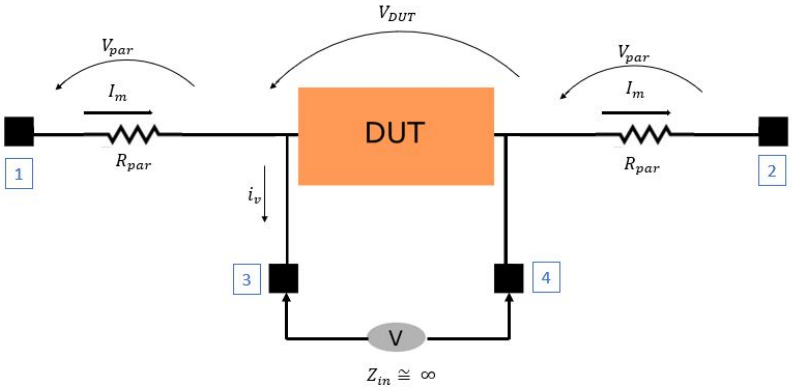

Figure 2.4: Four-terminal sensing measuring technique

By adding the pair of voltage-sensing electrodes (sense connections, number [3] and [4]), the lead and contact resistances can be removed from the measurement. Indeed, an Ohmmeter is used to sense voltage drop between sense connections. The Ohmmeter has an almost infinite internal resistance, which allows a very small current i_v through the sense connections and the Ohmmeter itself. Since the current is really small, the voltage drop coming from lead and contact resistances of sense connections will also be really small, and can therefore be neglected. The voltage drop measured by the Ohmmeter thus really represents the one around the DUT. This technique is also valid for impedance sensing, where the Ohm's law becomes $V = ZI$.

The voltage-sensing electrodes (sense connections) are placed as the inside pair, the closest possible to the device under test (DUT), and the current-carrying electrodes (force connections) are placed as the outside pair.

2.2 Electrode design

2.2.1 IDE working principle

Fringing field effect The fringing field effect in a non-ideality of parallel-plate capacitor. At the edges of the plates, because the electrical field lines have a closed behaviour, they tend to reach the other plate by creating circle arcs, since they are not directly facing the opposite plate (see Figure 2.5) This effect is used in interdigitated sensor to scan a substrate.

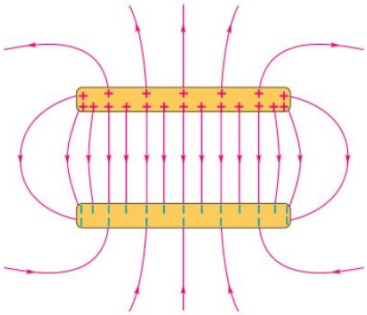

Figure 2.5: Fringing field effect on parallel plate capacitor [26]

If only parallel plates were use to sense capacitance in water, the sensed capacitance would be less than $10fF$ for $1cm^2$ of effective area and $1cm$ between the two plates, because of the large water permittivity. The only way to sense larger capacitances is to drastically increase the effective area while decreasing the space between the plates. Interdigitated electrodes are therefore the best suited structure for getting higher capacitance values using the same area on substrate [27].

An interdigitated sensor has the same working principle as a parallel-plate sensor. The only difference is that the electrical lines from the fringing field are the ones used for scanning the dielectric material. As shown in Figure 2.6(b) and (c), the electric field lines pass through the device under test (DUT), and the impedance between the electrodes can be measured. As the dielectric properties change with either physical, chemical or structural properties of the material, this measurement allows characterization of DUT with one-side access [28].

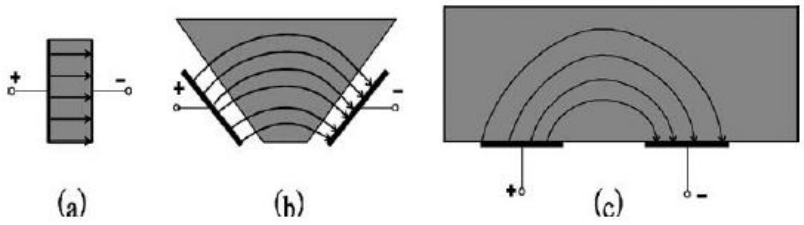

Figure 2.6: A fringing field sensor can be seen as a (a) parallel-plate capacitor whose (b) electrodes open up to provide (c) a one-sided access to the DUT [28]

Electrical field lines then penetrate into the material, with a depth proportional to the space between electrodes of opposite sign. The penetration depth is defined as the depth in which more than 90% of the field lines close. If the wavelength λ is taken as the space between two fingers belonging to the same electrode, the penetration depth is equal to $\frac{\lambda}{2}$. This parameter is assumed to be quasi-static and independent to frequency. It then only depends on geometrical parameters of the sensor.[28]

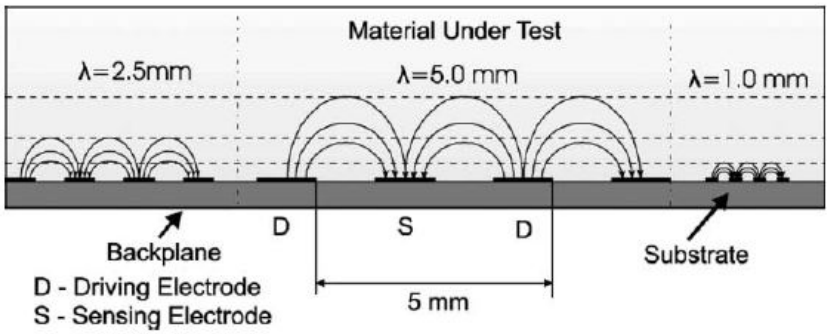

Figure 2.7: penetration depth of fringing field ($\frac{\lambda}{2}$) depending on wavelengths [28]

Using the fringing field effect on planar interdigitated electrodes present several advantages. The one-side access is useful to test a sample while the other side is electrode-free and thus allow absorption of gas, moisture or chemicals that might change electrical properties of the DUT. It is also a solution to sense a material when the other side is not accessible (i.e. human body) or too far away. The control of signal depth is also really interesting, and can serve for imaging when using multiwavelength interdigitated electrodes.

Unfortunately, fringing field effect on planar interdigitated electrodes also has drawbacks. One particularly to which we have to pay attention is that the field is going both ways. Since the 2 sensing electrodes are on the same plane, the fringing field effect appears on both the DUT side and on the substrate side. One way to make this effect marginal is to use a diffuse substrate so that the electrical lines diffuse into it, and thus do not reach the external environment

2.2.2 IDE structure dimensioning

The IDE structure has to be dimensionned in order to fit the application, meaning that it has to stay on the glabrous skin at the base of the thumb. Therefore, the sensing unit should not be much over $1cm^2$ of surface area so that it will not

face too much skin movement.
Since the sensor does not have to be stretchable, serpentine-shaped electrodes are not required, which greatly reduces the designing complexity.

2.2.2.1 Environment parameters

In order to capture the good range of capacitance, the IDE structure must be designed and dimensioned taking external parameters (size, permittivity, etc) into account. This was firstly estimated using the equation of capacitance between two parallel plates, adapted to take the number of fingers into account.

$$C = \frac{\varepsilon_0 \varepsilon_{r,sol} A_e}{W_s} (\frac{N_f}{2} - 1) \tag{2.1}$$

where ε_0 and $\varepsilon_{r,sol}$ are the vacuum and realtive liquid permittivity, A_e is the effective area, W_s the spacing between fingers and N_f the total number of fingers.

Permittivity The relative permittivity $\varepsilon_{r,sol}$ used in calculations is the permittivity of water, as a maximum value. The NaCl found in sweat indeed decreases the relative permittivity, because of the polarization of water molecules by ions it provokes. The more ions in the solution, the more polarized water molecules, the less free water molecules to allow current conduction [29]. Therefore, the permittivity is lower, since the amount of charges needed to generate one unit of electrical flux will be higher. As seen on the graph 2.8 just below, $\varepsilon_{r,sol}$ is decreasing linearly at the beginning, and then stabilizes around 45 when the NaCl concentration reaches 5M. In the case of sweat, the range of NaCl concentrations are between 10 and 100mM, so the relative permittivity value will be close to 80. As the cellulose pad is porous and contains around $1 - 2\%$ of material, we don't take the cellulose permittivity into account.

Conductivity [30] The conductivity σ_{sol} of a material or a solution is defined by its ability to carry an electrical current by the movement of charged particles [31].
Salts are ionic compounds that have a metal and a non-metal particle. The metal assumes a positive charge and is a cation, whereas the non-metal assumes a negative charge and is an anion. The attractive forces between the metal cation and the non-metal anion hold ionic compounds together as in solids. NaCl salt is water-soluble and dissolves into Na^+ cations and Cl^- anions in solution. The conductivity therefore increases with increasing salt concentration.
The conductivity is however not directly proportional to the salt concentration.

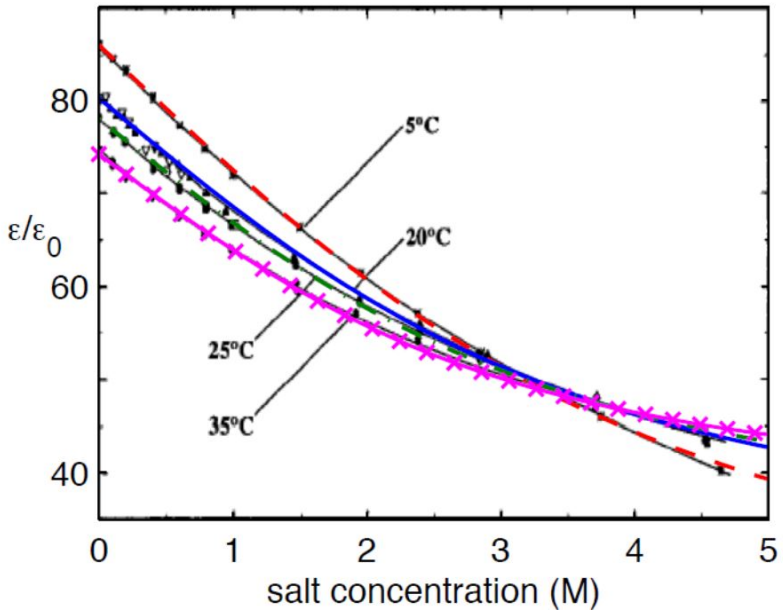

Figure 2.8: Relative permittivity of water depending on NaCl concentration [29]

Conductivity indeed depends on the number of charge carriers and their mobility. But number of charges and mobility are not independent properties: as the ions concentration increases, their mobility decreases. One can show that the conductivity thus increases linearly with respect to the square root of the NaCl concentration instead of a direct proportion: $\sigma_{sol} \propto \sqrt{[NaCl]}$.

Spacing of fingers For the distance W_s between the fingers, the working principle of the fringing field involves a penetration depth equal to the space between the electrodes.[32, 28] Since the cellulose pad is $0.4mm$ thick, the initial value we considered for W_s was $0.4mm$, in order to scan the whole cellulose pad. But in order to meet the scaling requirements, W_s was reduced to $0.3mm$.

Capacitance Based on literature [22], [23], the typical range of detected capacitances has been estimated to vary between $10 - 50pF$.

Having all these parameters, the dimensioning is performed by using the cell constant concept, which is a reliable way to relate geometrical parameters with environmental parameters.

2.2.2.2 Cell constant concept

A liquid solution can be represented as a parallel dipole of R_{sol} and C_{sol}. When putting the solution under electrical solution, the resulting Z_{sol} between the electrodes allows to find the conductivity σ_{sol} and permittivity ε_{sol} of the sensed liquid. This link is done using the equations $C_{sol} = \frac{\varepsilon_0 \varepsilon_{r,sol} A_e}{d}$ and $R_{sol} = \frac{d}{\sigma_{sol} A_e}$ where A_e is the effective area and $d = W_s$ is the distance between the 2 electrodes. By defining the cell constant c_k as the ratio between the electrode gap $d = W_s$ and their effective area, we obtain the following equation

$$c_k = \sigma_{sol} R_{sol} = \frac{\varepsilon_{sol}}{C_{sol}} = \frac{d}{A_e}$$

The cell constant therefore only depends on geometrical parameters of the sensor, and links the resistance R_{sol} with the conductivity σ_{sol}, as well as the capacity C_{sol} with the permittivity ε_{sol}. Choosing the geometrical parameters thus define the detection range of the conductivity and permittivity.

$$c_k = \frac{1}{(N_f - 1)L_f} \frac{2K(k)}{K(\sqrt{1-k^2})} \tag{2.2}$$

$$K(k) = \int_0^1 \frac{dt}{\sqrt{(1-t^2)(1-k^2t^2)}} \tag{2.3}$$

$$k = cos(\frac{\pi}{2} \frac{W_f}{W_s + W_f}) \tag{2.4}$$

As the variation range of permittivity is really low compared to the one of conductivities, the value of the cell constant will be estimated using permittivity and the range of capacitances found in literature. Using the equations (2.2), (2.3) and (2.4), we can optimize the geometrical parameters of the IDE sensor by taking the sensor surface ($\approx 1cm^2$) into account. These parameters are put together in Table 2.1. Note that these equations are simplifications, because they do not take the electrode thickness into account. They also consider the fringing electrical field to be elliptic between 2 electrodes [27].

The cell constant is defined using a relative permittivity $\varepsilon_{r,sol} = 80$ and a solution capacitance $C_{sol} = 50pF$. The expected cell constant is therefore: $c_k = \frac{\varepsilon_{sol}}{C_{sol}} = \frac{\varepsilon_{r,sol}\varepsilon_0}{C_{sol}} = \frac{80 \cdot 8.854 \cdot 10^{-12}}{50 \cdot 10^{-12}} = 14.17$. Using the expressions (2.2), (2.3) and (2.4) and the applied geometrical parameters in Table 2.1, we get a real cell constant $c_k = 14.49$, which is close to the expected one.

Name	Symbol	Value	Units
liquid relative permittivity	$\varepsilon_{r,sol}$	80	-
liquid capacitance	C_{sol}	10-50	[pF]
finger width	W_f	0.4	[mm]
spacing width	W_s	0.3	[mm]
finger length	L_f	8.3	[mm]
total finger number	N_f	16	[-]
electrode height	h_f	100	[nm]

Table 2.1: Geometrical parameters of the sensor obtained thanks to cell constant equations (2.2), (2.3) and (2.4)

2.3 Material selection

Electrode material For such application, we choose to use gold because of its biocompatibililty. The inert properties of gold are also attractive, since it has a really low tendancy to metal corrosion and to electrical double layer (EDL) formation. In order to deposit gold on the substrate, a thin layer of either Ti or Cr is needed as adhesive layer. We opt for Ti because of its biocompatibility.

Substrate material Flexible polymers are selected as substrate because of their thermal stability, chemical resistance or good mechanical flexibility. The most used flexible substrates in wearable electronics are polyimide, PDMS and PET. Their characteristics are found in Table 2.2 below.

As explained in section 2.1.1, the decision was made to create a flexible sensor. PDMS is therefore not the best option. The hydrophobic surface and the poor thermal stability don't encourage to take this substrate, although it is often used in biomedical applications because of its biocompatibility. PDMS is also known to absorb water over a long time, which is clearly not ideal in this application.
PEN and PET also have to be excluded because of their water absorption.
A $50\mu m$ Kapton ®polyimide film is thus used because of its good flexibility, high thermal stability and high tensile strength.

Absorbent pad Cellulose is selected as absorbent material because it is a natural and biocompatible porous material which has good capillary absorption capacities. In the literature, the collecting pad are often around $1mm$ thick. Choosing a thinner pad allows to have a faster detection of sweat as well as an easier design of the sensor. Having a $1mm$ thick pad indeed entails a finger spacing $W_s = 1mm$, which leads to larger sensor dimensions and thus makes the fit on the glabrous

Material	Strechable/ bendable	Thermal stability	Pros	Cons
Polyimide (PI)	Bendable	up to 452°C	high tensile strength, resists weak acids, alkalis and organics solvents	low transparency
polyethylene terephtalate (PET) and polyethylene naphthalate (PEN)	Bendable	PET <100°C, PEN <180°C	transparent (>85% of visible wavelengths)	easily permeated by oxygen and water (water absorption≈ 0.14%), poor stretchability due to high modulus of elasticity (2-3GPa)
PDMS (Silicone)	Stretchable	<100°C	biocompatibility and intrinsic high stretchability	thermal expansion, hydrophobic surface, need treatment for adhesion

Table 2.2: characteristics of usual flexible substrates in wearable electronics [33]

skin even more difficult. The absorbent pad is here therefore limited to $0.4mm$ thick.

2.3.1 Passivation layer

The passivation layer is used to create an insulating barrier between the electrode metal and the cellulose pad. This encapsulation allows a capacitive measurement by cutting the DC path between the fingers in presence of water, since the water has a finite conductivity. The passivation layer also allows to remove solid-liquid interface effects such as faradaic current or electrical double layer:

A. Faradaic current appears whenever there is a charge transfer between solid and electrolyte, and is due to redox reactions.

B. The electrical double layer (EDL) is created at the solid-liquid interface, and has two different layers. The first one, the closest to the solid, is formed of ions attracted by the electrode with opposite charge, causing a really compact layer at the solid-liquid interface. The second one, called the diffuse layer, is composed of ions attracted by the surface charge of the first layer, as represented on Figure 2.9. Since the typical EDL thickness rarely exceeds a few nanometers, the electrical double layer capacitance C_{dl} has a very high capacitance value, and its influence is quickly lowered when the sensing cells dimensions exceeds a few microns [27]. When using an insulating layer, since the EDL capacitance C_{dl} and the insulating layer capacitance C_{ins} are in series, C_{dl} is screened by C_{ins}.

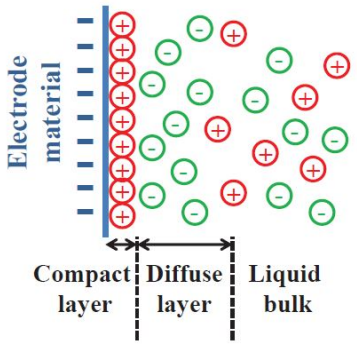

Figure 2.9: Electrical double layer phenomenon [27]

The passivation layer is here done using Atomic Layer Deposition (ALD) of Al_2O_3. ALD allows a really precise control on the thickness of the layer, since the method has a resolution of $1Å = 0.1nm$. We indeed need the passivation layer to be as small as possible, in order to have a greater impact of the liquid presence in the sensitive area. Having a small passivation layer is also required to meet the flexiblity requirement.

2.4 Fabrication process

2.4.1 Sensor unit fabrication

Laser cutting The first step in order to get a proper design for the sensor was to obtain a mask. We choose to use laser cutting because the dimensions allow it, it is cheaper and make the redesign easier than with a lithogaphy mask.

By first using a $50\mu m$ sheet of Nickel, it was impossible to keep the negative part of the sensor, i.e. the mask, intact, because it was too delicate. Fortunately, by just switching from $50\mu m$ to $100\mu m$ Ni sheet, we are able to obtain a nicely cut mask. Using $100\mu m$ sheet, we slowly decreased the laser height to cut the whole sheet thickness at maximum focus (see Figure 2.10).

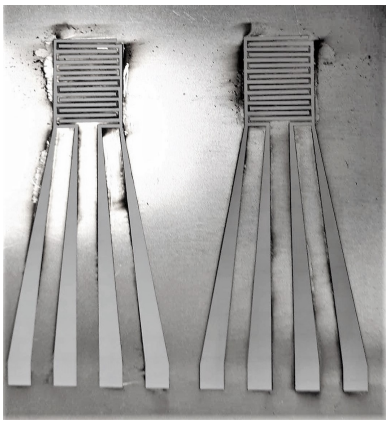

Figure 2.10: Mask obtained thanks to laser cutting into a Ni sheet

Electron beam deposition Titane ($10nm$) is first deposited on polyimide film for adhesion of gold on the polyimide film, and then a $100nm$ layer of gold is deposited as electrode metal. Both depositions are made with Electron Beam Deposition.

Atomic layer deposition The deposition of an Al_2O_3 insulating layer is done by sequential surface reactions of $Al(CH_3)_3$ (trimethylaluminium TMA) and water. As it happen one atomic layer at the time, the number of cycles defines the thickness of the layer. Here, we have applied 200 cycles to reach a thickness of $20nm$.

2.4.2 Pad connection

In order to properly connect the sensor to the measurement device without creating too much noise and parasitic effects, the cable length has to be minimized. Some really small copper wires were soldered directly onto the pads with a precise temperature to make the tin melt while conserving the gold material. These copper wires allow an easy coupling to any measurement device.
Since the connection pads will be in contact with skin, they need to be covered by an insulating layer to remove impact from skin on the measurements at this location. To do so, UV insulating epoxy was deposited around the exposed connection pads and copper wires, as shown on Figure 2.11.

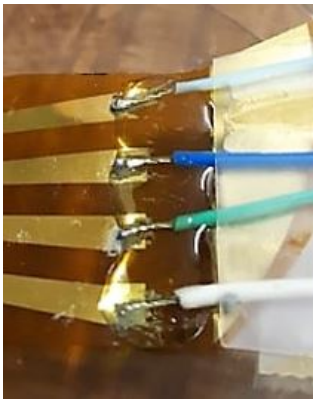

Figure 2.11: UV epoxy deposited on welds

2.4.3 Sensor-absorbent pad interface

For the interface between the sensor and the cellulose pad, the implemented easy solution is to use Kapton ®tape to stick the polyimide film around the sensor and the cellulose pad together.

2.4.4 Skin-sensor interface

To hold the sensor properly on the skin, a 3M™Tegaderm™bandage as shown on Figure 2.12 is a viable option quite often used in the literature [18], [22], [23]. It allows a good skin respiration while sticking to the skin. The transparent silicone part could also play the role of a backing layer, which will scatters the external electrical lines of the IDE structure, prevent them of sensing the external environment (see section 2.2.1), and therefore make sure that the changes in absorbent pad are the only ones observed and interpreted.

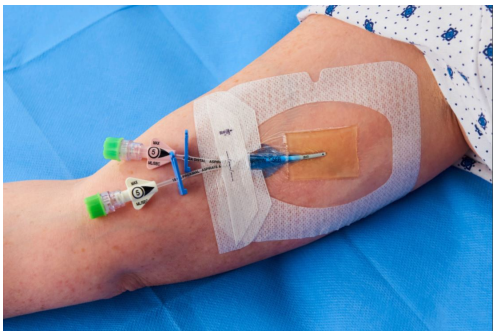

Figure 2.12: Example of a 3M™Tegaderm™adhesive bandage [34]

2.4.5 Final product and assembly

After all fabrication steps, the result can be seen on Figure 2.13. The first test in section 3.3.1 was run using the sensor on poylimide sheet without welded copper wires. The other tests in section 3.3.2, 3.5, 3.4 and 3.6 were run using the assembly presented on Figure 2.14, with or without absorbent pad depending on the test objective.

Figure 2.13: IDE sensor final product

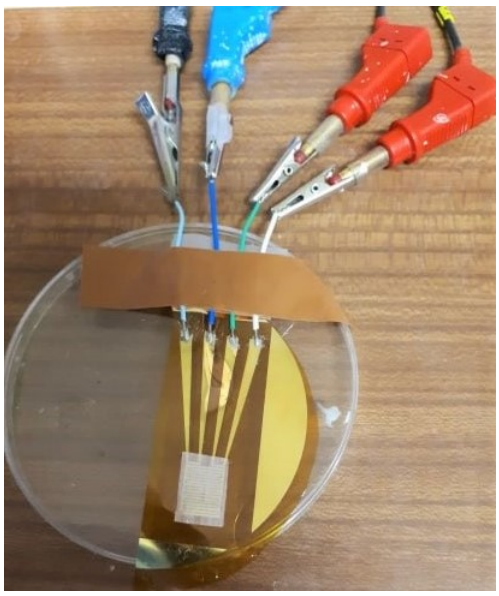

Figure 2.14: Assembly of the sensor for experimental validation

Chapter 3

Experimental validation

3.1 Equivalent electrical model

The electrical equivalent circuit can be extracted from Figure 3.1, assuming that the sensed liquid can be represented as a $R_{sol} - C_{sol}$ parallel dipole, and the insulating layer as a capacitance C_{ins}. As explained in section 2.3.1, the insulating layer makes the cell non-faradaic, and we can therefore neglect solid-liquid interface effects. The electrical doubler layer capacitance C_{dl} can be neglected as well because it is screened by the insulating layer capacitance, since there are in series. From the circuit in 3.1, we can deduct the equivalent impedance (3.1),

$$Z_{IDE} = \frac{1}{(j\omega C_{ins})} + \frac{R_{sol}}{(1 + j\omega R_{sol} C_{sol})} \tag{3.1}$$

where C_{ins} represents the sum of two passivation capacitances by which the electrical lines have to go through.

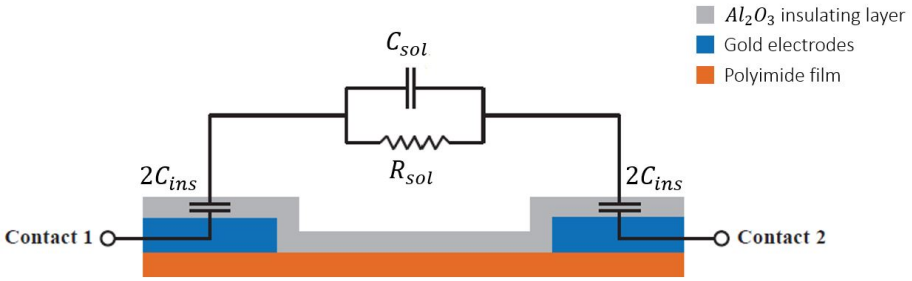

Figure 3.1: Equivalent electrical model (not on scale, adapted from [27])

By transferring the impedance equation into the Laplace domain, it is possible to predict the behaviour of the Bode diagram. Using the equations (3.2), (3.4), (3.3), we can say that the bode digram will start with a decreasing slope linked to $\frac{1}{sC_{ins}}$, then will have a flat zone because of the zero at ω_z and decrease once again because of the pole at ω_p, since $\omega_z < \omega_p$.

$$Z_{IDE} = \frac{1}{sC_{ins}} \frac{(s + \omega_z)}{(s + \omega_p)} \tag{3.2}$$

$$\omega_z = \frac{1}{R_{sol}(C_{sol} + C_{ins})} \tag{3.3}$$

$$\omega_p = \frac{1}{R_{sol}C_{sol}} \tag{3.4}$$

The two negative slopes therefore relate capacitive behaviours, while the flat region represent the solution resistance R_{sol}.

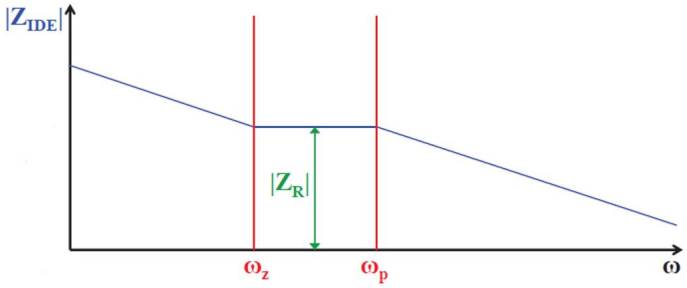

Figure 3.2: Expected Bode plot behaviour [27]

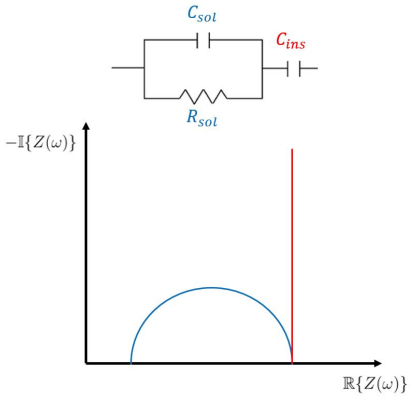

Figure 3.3: Expected Cole-Cole plot behaviour

The Cole-Cole plot of this equivalent circuit will behave as shown on Figure 3.3. A semi-circle on a Cole-Cole plot represents a parallel R-C dipole, since both the real part and the imaginary part of the impedance vary with frequency. The right end of the semi-circle matches the DC path, when frequency is too small and the capacitance stays charged, and is therefore considered as an open wire. At the left end, the frequency is larger and make the capacitance negligible, which thus acts as an short-circuit.

The vertical line corresponds to a serial capacitance : whatever the frequency, the real part is fixed and only the imaginary part varies.

3.2 Flexural strength of insulating layer

The ALD layer is deposited in order to have an insulating barrier between the cellulose pad and the electrodes. We need this encapsulation to allow proper capacitive measurements and the removal of solid-liquid interface effects. Otherwise, some chemical reactions would occur at the interface and would perturb the measurement.
But even if the Al_2O_3 layer is really thin, it's not known to be really flexible. Therefore, some tests with the potentiostat were run, to check whether if the ALD layer can support flexibility constraints. Atomic Force Microscopy(AFM) would have giving us information about surface evolution after constraints, but not about the functional nature of the layer. This is why impedance spectroscopy using a Potentiostat with Frequency Analyzer Module (Metrohm Autolab PGSTAT302N [35]) is the best tool for this specific purpose. It will indeed react differently if the layer kept its integrity and is still waterproof, or if it has been cracked and lets the water and ionic species pass through.

3.2.1 Impedance spectroscopy operating principle

To perform impedance spectroscopy, an electrochemical cell, an impedance analyzer and eventually a potentiostat are the key elements. The impedance measurement is done between the working electrode (WE) and the counter electrode (CE). The reference electrode (RE) is used to maintain a constant potential thanks to a potentiostat, and is thus not needed when no electrochemical reactions occur in electrolyte [36]. Generally, when the electrolyte is a NaCl solution, the reference electrode is made of Ag/AgCl. But since we do not have redox reactions happening thanks to the insulating layer, we can use a pseudo-reference electrode made of platinum.

The obtained plots considered here give information about the electrical behaviour of the elements between the working and the counter electrodes. As the impedance can be written in 2 different ways, the equipment software will give 2 kinds of graphs.

$$Z(\omega) = |Z(\omega)| \cdot e^{j\theta_z(\omega)} \tag{3.5}$$

$$Z(\omega) = \mathbb{R}\{Z(\omega)\} + j\mathbb{I}\{Z(\omega)\} \tag{3.6}$$

where $|Z(\omega)|$ is the impedance modulus and θ_z is the impedance phase.

On the one hand, the Bode plot represents the impedance modulus $|Z(\omega)|$ and the phase θ_z with regard to the frequency. On the other hand, the Nyquist plot,

also called Cole-Cole plot, represents $-\mathbb{I}\{Z(\omega)\}$ in regard to $\mathbb{R}\{Z(\omega)\}$.

To give an example, Figures 3.4(b) and 3.5 are respectively the Cole-Cole plot and the Bode plot for the circuit represented on Figure 3.4(a).

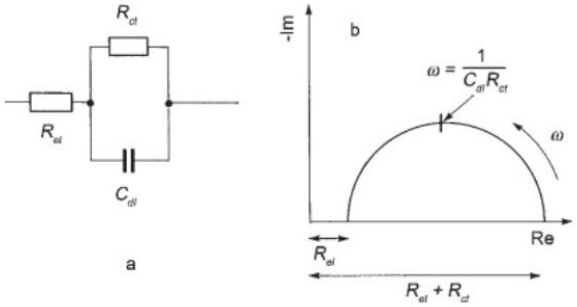

Figure 3.4: (a)electrical circuit R+(R//C) (b)Cole-Cole plot of the circuit [37]

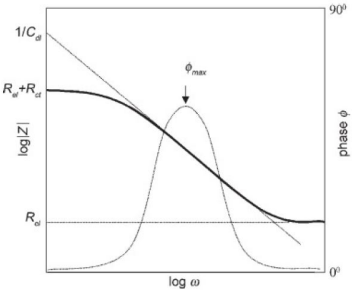

Figure 3.5: Bode plot of a R+(R//C) circuit [37]

This circuit on Figure 3.4 is used when representing an electrochemical cell. The first resistance in series R_{el} is the electrolyte resistance. The resistance R_{ct} on the parallel dipole is called the charge-transfer resistance, and is found whenever there is an electron exchange between the 2 electrodes. The capacitance C_{dl} represents the electrical double layer effect.

In this thesis context, since there is a passivation layer, the electrical double layer capacitance is screened by the one of the insulating layer. The sensing information is thus mainly contained in dielectric properties of the system. The same equivalent electrical circuit can thus be used by only replacing C_{dl} with C_{ins}, the capacitance of the insulating layer.
Using a passivation layer also causes the cell to be non-faradaic, meaning that it is supposed to have no electron transfer at solid-liquid interface. The charge-transfer resistance R_{ct} will therefore be removed from the equivalent circuit. This is the property used to test the passivation layer integrity of the sensor.

The goal of such test is indeed to observe whether the passivation layer keeps its insulating properties after being bent, which is crucial for the objective of this thesis. If it is not damaged, the encapsulation will stay intact, and therefore no electron transfer would occur at solid-electrolyte interface, so no R_{ct} should be observed.

That information can be easily deducted from the Cole-Cole plot. On Figure 3.6, the cell is capacitive, there is no charge transfer at the solid-liquid interface.

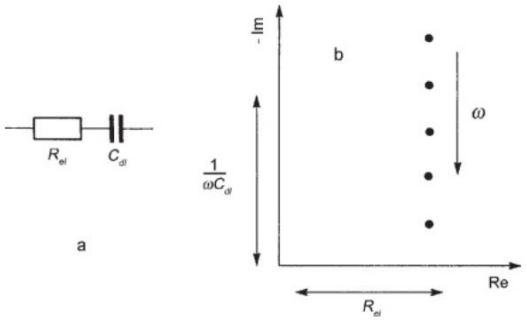

Figure 3.6: Cole-Cole plot of a R+C circuit [37]

Therefore, the vertical line representing the capacitance is offset by the solution resistance. If some resistive path between the liquid and the electrode metal were to appear, the Cole-Cole plot would look like the one on Figure 3.4, where there is a charge transfer resistance. Such resistance involves both the real and imaginary parts of impedance to vary with frequency.

The expected results are comparable to Figure 3.6, with the resistance R_{el} being the one of the NaCl solution, and the capacitance the one of the passivation layer. If the insulating properties are lost after bending, cracks in the Al_2O_3 layer will open a path for the electrons to reach the electrode metal, and a charge transfer resistance will appear, as on Figure 3.4.

3.2.2 Experimental setup

Some $50\mu m$ Kapton®polyimide pieces, wiped with isopropanol, were deposited with Ti ($10nm$) and Au ($100nm$) with Electron Beam Deposition over the whole surface to mimic the actual layers of the sensor. Then, using an Atomic Layer Deposition technique, the deposition of Al_2O_3 ($20nm$) was made, letting one part of the Au electrode exposed (see the right side on Figure 3.7). Then, it was placed in the measurement cell as on Figure 3.8.

A 100mM NaCl solution [1] is placed in the central hole. The concentration is chosen to match the range of NaCl concentration in sweat. There is no joint on the other side of the polyimide sheet, in order to minimize the constraints applied on the DUT by the joints when tightened. Since there are no redox reactions, there is no need for an Ag/AgCl reference electrode. The ALD-covered surface is placed

[1] A 0.5M NaCl solution were dissolved to obtain the wanted concentration

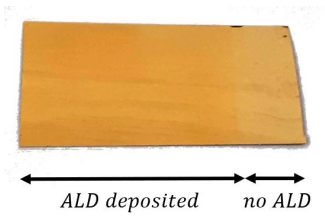

Figure 3.7: polyimide-based sheet for flexibility tests, coated with Al_2O_3

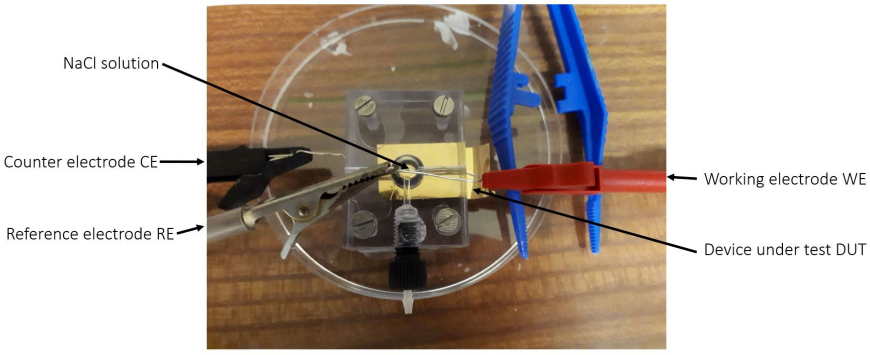

Figure 3.8: Set up for flexibility tests

below the hole, and the exposed part is attached to the counter electrode thanks to a crocodile clip. The reference electrode is the closest to the DUT. Both the counter and the reference electrodes are in contact with solution through holes in the measurement cell. This measurement cell is used to ensure a stable position of the electrodes relative to each other, because a change in distance between them will alter the measurement.

The voltage imposed by the equipment must be smaller than $26mV$, which is the thermal voltage. It is defined as $V_T = \frac{kT}{q}$ where T is the absolute temperature (300K), k is the Boltzmann constant and q is the charge of an electron [38]. This precaution is made to avoid passing through the passivation layer, and to assume the system as linear.

Between every measurement, the DUT is wrapped around a tube in order to inflict a homogen bending constraint on the DUT. The tube diameter is progressively reduced to observe a potential crack in the ALD layer with increasing bending constraint. The tubes diameter are, in the descending order: 4cm, 3.2cm, 1.6cm, 1.2cm, 1cm and 0.8cm. Unfortunately, the pressure imposed by the joint on the ALD layer was too strong and was destroying it. Therefore, only 2 tests (at different places) were possible with one little polyimide sheet. Since several polyimde sheets were deposited, measurements were still possible.

3.2.3 Results

The first test is done with unfolded sheet where no bending constraint were applied, to observe the basis characteristics of the insulating layer. The stimulation

is made between 1 and $10kHz$, with a peak voltage of $10mV$.

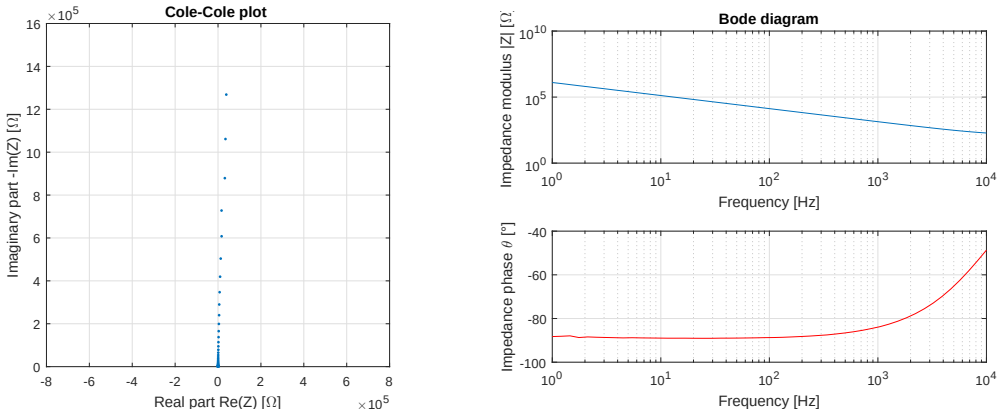

(a) Cole-Cole plot of unfolded DUT **(b)** Bode plot of unfolded DUT

Figure 3.9: Test №1: unfolded DUT

Both the vertical line on the Cole-Cole plot (Figure 3.9a) and the negative slope on the amplitude Bode plot (Figure 3.9b) represent a capacitive behaviour, as expected. Figure 3.10 is a zoom of the Cole-Cole plot of the unfold sheet, and

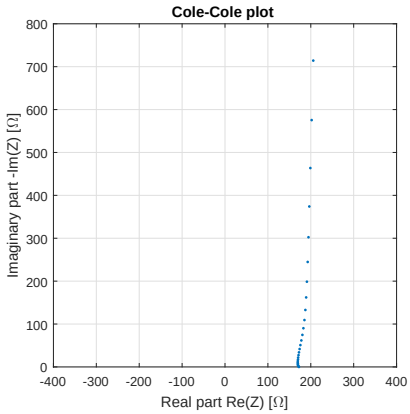

Figure 3.10: Zoom on the Cole Cole plot of unfolded DUT

it appears that the vertical line is offset by approximately 200Ω, which can be interpreted as the solution resistance, as seen on Figure 3.6. Both plots on Figure 3.11 and the Cole-Cole plot on Figure 3.12 show that the DUT behaviour stays the same no matter the bending constraint.
On Figure 3.13, a sweep frequency range of $[20Hz - 1MHz]$ is shown. This allows to observe the DUT behaviour at high frequencies.

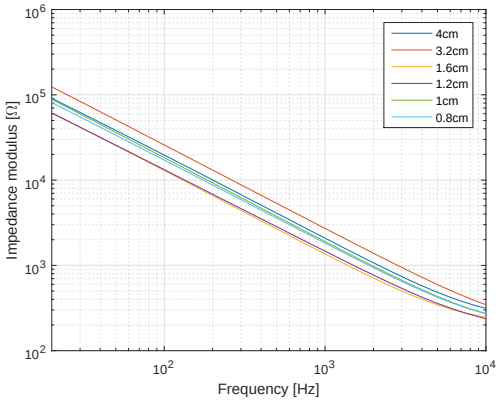

(a) Impedance modulus Bode plot

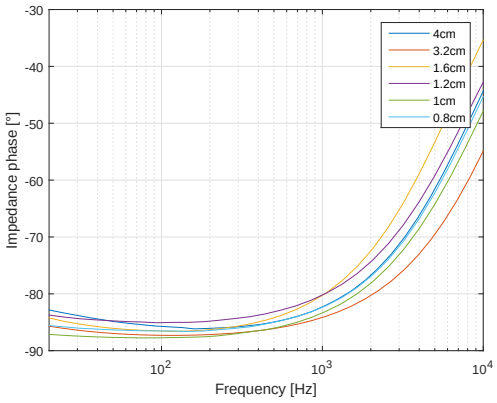

(b) Impendance phase Bode plot

Figure 3.11: Bode plots corresponding to DUTs subject to bending constraint

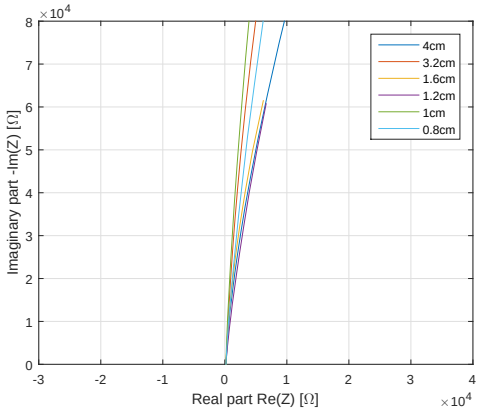

Figure 3.12: Cole-Cole plots corresponding to DUTs subject to bending constraint

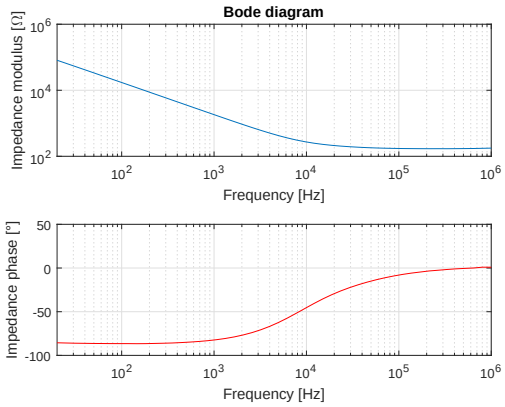

Figure 3.13: Bode diagram of extented frequency range

3.2.4 Interpretation

The Table 3.1 summarizes the battery of tests. It can be seen that the frequency range was changed in the middle of the experiment. This was done to match the frequency range of the LCR meter, but since the number of experiments was limited because of the degradation of the DUT by the joint, it was not possible to re-run the first tests. This fact however does not affect the results.

The results are very promising. On every Cole-Cole plot, the line stays more or less vertical, which means that the capacitive behaviour subsists despite the

Test name	Tube diameter	Start frequency	Stop frequency
Test №1	no tube	$1Hz$	$10kHz$
Test №2	4cm	$1Hz$	$10kHz$
Test №3	3.2cm	$1Hz$	$10kHz$
Test №4	1.6cm	$20Hz$	$1MHz$
Test №5	1.2cm	$20Hz$	$1MHz$
Test №6	1cm	$20Hz$	$1MHz$
Test №7	0.8cm	$20Hz$	$1MHz$

Table 3.1: Recapitulative table of the test battery

bending constraints. Because of the existing curvature radius in some of the tests, there can be a doubt regarding the presence of a resistive path. But this radius is so big that it can be interpreted as a $M\Omega$ resistance, which thus allows a negligible current at its accesses.

On Figure 3.13, we can observe a flat line at high frequencies. This flat line is related to the electrolyte resistance. At high frequencies, the capacitance becomes a short-circuit, and the only remaining component is thus the resistance.

3.3 Calibration

3.3.1 Probe sensing

Using the Prober MPI 300mm [39], preliminary sensor results are obtained. Their goal is to observe the order of magnitude of the tare capacitance. $50mV$ AC potential was applied over a frequency range from $1kHz$ to $1MHz$. An open calibration was first executed in order to remove all parasitic capacitances associated to the devices leads and contacts. The probes were then put on the connection pads of the sensor and a first test was run using the "empty" sensor (test run on both deposited sensor units). Then the cellulose pad has been added on the IDE structure surface, and the test is run again. The impact of the cellulose pad covering the electrode fingers on capacitance measurement can also be observed.

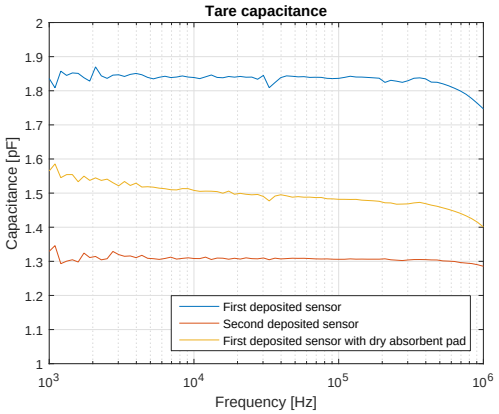

Figure 3.14: Sensed tare capacitance using a probe system

	G_p
First sensor	$2.77[nS]$
Second sensor	$4.81[nS]$
With dry absorbent pad	$154[\mu S]$

Table 3.2: Mean conductance value $G_p[S = \frac{1}{\Omega}]$

Following the results on Figures 3.14, the sensor had a tare capacitance around $1.5pF$. This is negligible compared to expected capacitance variation range ($[10 - 50pF]$).

When adding the cellulose pad, the sensed capacitance does not significantly vary from the tare capacitance. This confirms the hypothesis saying that the cellulose pad can be neglected in impedance analysis, and that only the liquid shall influence the results.

As seen on Table 3.2, the conductance values for the three measurements have an order of magnitude around the $[nS] = 10^9[\Omega]$ because of $[S = \frac{1}{\Omega}]$. This measurement thus allows to understand that there is no DC path on the tare capacitance, meaning that the metal deposition was well-made.

3.3.2 Impact of additional connection cables

To allow the connection between the sensor and the measurement device, additional routes and cables are used. These routes (small copper wires) will eventually perturb the impedance measurement, and their impact has to be analysed. To do so, a tare test with no solution on the cellulose pad is run using the Autolab Potentiostat [35], as presented on Figure 2.14, but without pad.

On the Figure 3.15, a straight line with negative slope is observed on the impedance modulus plot, and a phase around 90° for the impedance phase plot. The Cole-Cole plot on Figure 3.16 shows a vertical line.

When the cellulose pad is dry, the sensed impedance is purely capacitive, since there is no R-C parallel dipole from electrolyte presence. The negative slope of Bode plot on Figure 3.15 and the vertical line of Cole-Cole plot on Figure 3.16 both

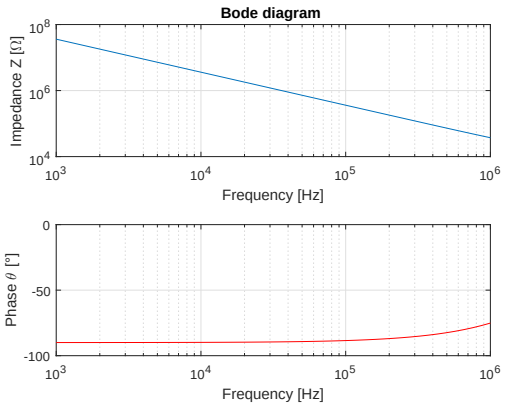

Figure 3.15: Bode diagram executed with no solution on cellulose pad

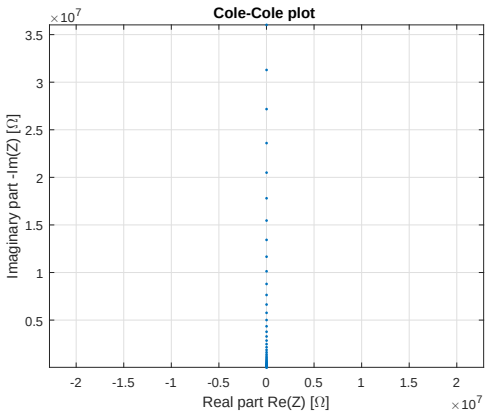

Figure 3.16: Bode diagram executed with no solution on cellulose pad

clearly reflect capacitive behaviour. The sensed capacitance is measured around $3 - 5pF$, depending on the connection wires.

The lead parasitic effects, both from the copper leads and the tracks on polyimide, can not be removed with open calibration since they are soldered on the device. But fortunately, this capacitance value is still small compared to the variation range, and therefore does not influence the measurement. According to the phase plot on Figure 3.15, there is also no resistance, or at least the resistance is negligible, since the impedance phase is really close to $\theta_z = -90°$.

3.4 Changes in salt concentration

In this section, the results are obtained using the Metrohm Autolab Potentiostat [35]. $50mV$ AC potential is applied over a frequency range from $1kHz$ to $1MHz$, as the device is limited to $1MHz$.

A new cellulose pad is used for each experiment, to avoid contamination. The pad is submerged into a specific NaCl solution, and then placed onto the interdigitated structure to mimic sweat generation. Four different NaCl concentrations are tested: de-ionized water ($0mM$), $10mM$, $50mM$ and $100mM$, as the variation range of NaCl concentrations in human sweat is $[10 - 100mM]$ (see section 1.1.2.1 for further details). Between every measurement, the sensor is washed with DI water and dried to avoid alterations in the measurement.

3.4.1 Results

Figures 3.17 and 3.18 show a comparison of bode plots between the different NaCl concentrations.

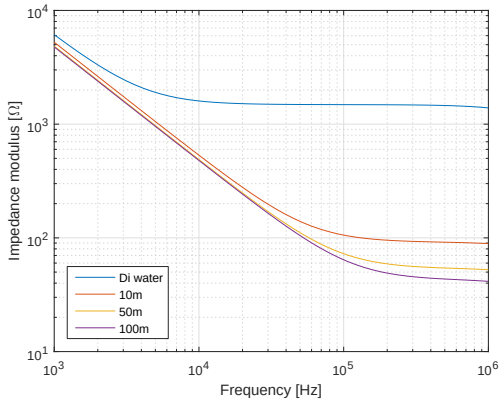

Figure 3.17: Comparison of impedance modulus for different NaCl concentrations

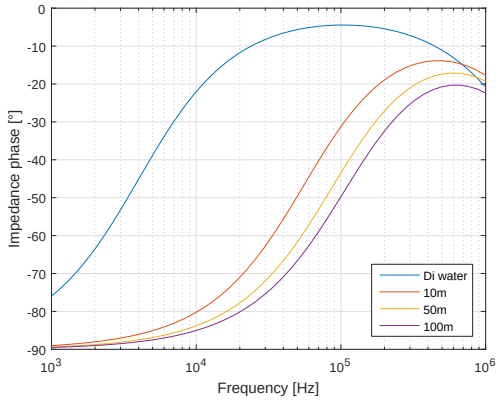

Figure 3.18: Comparison of impedance phase for different NaCl concentrations

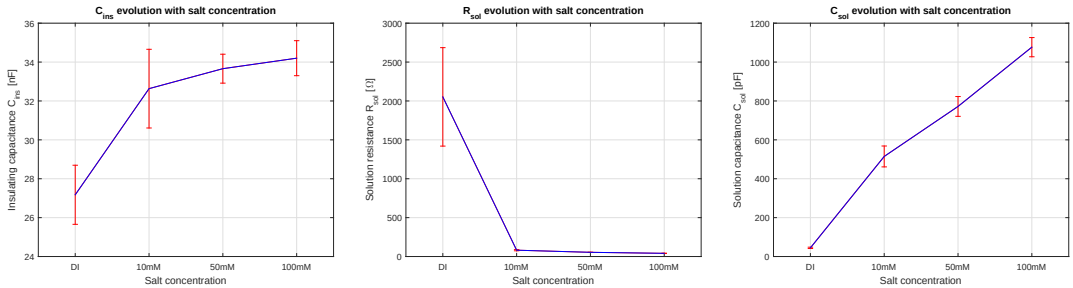

(a) C_{ins} evolution with increasing salt concentration

(b) R_{sol} evolution with increasing salt concentration

(c) C_{sol} evolution with increasing salt concentration

Figure 3.19: Evolution of component values obtained by fitting for different salt concentrations, based on Table B.1

On Figure 3.17, the difference between deionized water and saline water can clearly be observed. But more importantly, the impedance modulus corresponding to the flat region of the plot decreases with increasing NaCl concentrations, which is therefore a way to discriminate between the different solutions. On Figure 3.18, the difference between the different plots is also present, showing a decreasing value for the phase maximum with increasing salt concentrations.
The cut-off frequency also increases with increasing salt concentrations.

The plots 3.19 puts together all components values obtained with the *Fit and Simulation* option of the Autolab Potentiostat. Although the fitting might contain some inherent measurement errors, it gives a good overview of tendencies.

3.4.2 Interpretation

The solution resistance is linked to the conductivity by the cell constant $c_k = \sigma_{sol} R_{sol} = \frac{d}{A_e}$. Since the cell constant is fixed by geometrical parameters, the solution resistance is inversely proportional to the conductivity. As the conductivity varies as follows: $\sigma_{sol} \propto \sqrt{[NaCl]}$ (see section 2.2.2.1), the solution resistance is expected to decrease with increasing conductivities and salt concentrations. To observe the resistance behaviour, we have to take a look at the flat region in impedance modulus plot. When R_{sol} decreases, $|Z_{IDE}|$ decreases, and the flat region $|Z_R|$ is lower. The decreasing tendency is also visible on the plot 3.19b, with a solution resistance for de-ionized water two order of magnitudes higher than with saline water. As the conductivity raises with the number of mobile charged particles because of their ability to carry current, it is normal that the de-ionized solution resistance is high, reflecting poor conductivity.

The maximum phase value decreases with increasing salt concentration because of the relationship $tan\theta_z = \frac{Im(Z)}{R(Z)}$.

An important observation has been made on the cut-off frequencies. Because of the expression $f_z = \frac{1}{2\pi R_{sol}(C_{ins}+C_{sol})}$, and since C_{ins} basically remains the same and the changes in C_{sol} are shadowed by C_{ins} ($C_{ins} >> C_{sol}$), the cut-off frequency is dominated by R_{sol} evolution. Whenever R_{sol} decreases, f_z increases. Because of such predominance of R_{sol} concerning cut-off frequencies, an important issue takes place concerning the observation of the whole impedance evolution in saline water. The order of magnitude of saline cut-off frequencies can be estimated as (3.7) and (3.8) using the values of Table B.1.

$$f_z = \frac{1}{2\pi R_{sol}(C_{ins} + C_{sol})} \approx \frac{1}{2\pi 10^1 (3 \cdot 10^{-8} + 4 \cdot 10^{-10})} \approx 10^6 \tag{3.7}$$

$$f_p = \frac{1}{2\pi R_{sol} C_{sol}} \approx \frac{1}{2\pi 10^1 \cdot 4 \cdot 10^{-10}} \approx 10^8 \tag{3.8}$$

This means that the second cut-off frequency f_p will not be observable using the measurement devices available (which are limited to $1MHz$). Keeping this fact in mind, it also explains the unexpected solution capacitances values obtained during the fitting step (see plot 3.19c). It happens indeed, while looking at the expression

of the sensed impedance (3.9),

$$Z_{IDE} = \frac{1}{(j\omega C_{ins})} + \frac{R_{sol}}{1 + j\omega R_{sol} C_{sol}} \tag{3.9}$$

that the term $j\omega R_{sol}C_{sol}$ is shadowed by 1 whenever R_{sol} or ω are too small, regardless of C_{sol} being either $\approx 10^{-12}$ or $\approx 10^{-10}$. This explains why the *Fit and Simulation* option is so likely to give big values of C_{sol} in saline water, because it is not able to properly approach the real value with limited frequency $\omega = 2\pi f$.

Despite of this issue on the cut-off frequencies visibility, the intended objective of discrimination with regards to NaCl concentration is well completed, using the flat region of modulus plot and the maximum value of the phase plot with values intervals corresponding to salt concentration.

3.5 Equivalent electrical circuit validation

The goal of this test is to validate the equivalent electrical circuit presented in section 3.1. To do so, the behaviour of both Bode plot and Cole-Cole plot are studied. Thanks to the Autolab Potentiostat [35], impedance spectrscopy is realized by applying a $50mV$ AC potential over a frequency sweep from $1kHz$ to $10MHz$. This bandwidth is chosen to allow a full and complete observation of both the modulus and the phase bode plots. Thanks to the components value collected during the test in section 3.4, we are able to estimate the order of magnitude of cut-off frequencies. Those of de-ionized water are indeed :

$$f_z = \frac{1}{2\pi R_{sol}(C_{ins} + C_{sol})} \approx \frac{1}{2\pi 10^3 (3 \cdot 10^{-8} + 4 \cdot 10^{-11})} \approx 10^4 \tag{3.10}$$

$$f_p = \frac{1}{2\pi R_{sol} C_{sol}} \approx \frac{1}{2\pi 10^3 \cdot 4 \cdot 10^{-11}} \approx 10^7 \tag{3.11}$$

However, since the bandwidth of both the LCR meter and Autolab Potentiostat ends at $1MHz$, we expect that going over this threshold will introduce some errors in measurement. Even if the potentiostat can be forced over this bandwidth, the generated errors will strongly affect the *Fit and Simulation* option available on the device. For that reason, only this test will be performed with a broad frequency of $1KHz$ to $10MHz$.

Moreover, the choice to observe de-ionized water over saline water is pratically imposed by the limited frequency bandwidth of both devices. Indeed, given the

expression of cut-off frequencies above and the results obtained by experiment, the whole behaviour of both Bode plots cannot be fully observed for saline water, as explained in section 3.4.

3.5.1 Results

Figures 3.20, 3.21 and 3.22 show the results obtained with the cellulose pad submerged in de-ionized water.

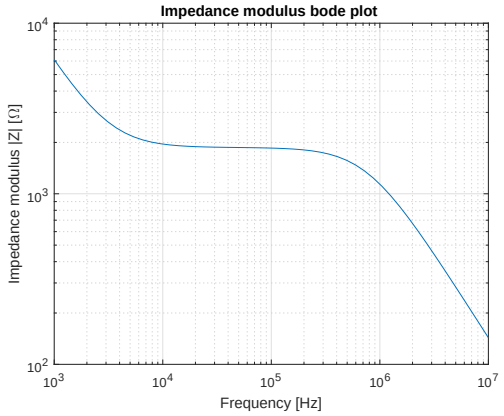

Figure 3.20: Impedance modulus bode plot when de-ionized water on the cellulose pad

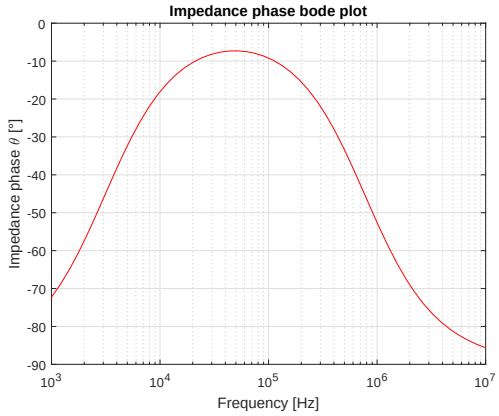

Figure 3.21: Impedance phase bode plot when de-ionized water on the cellulose pad

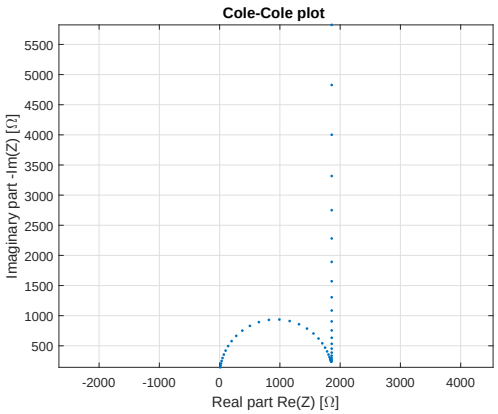

Figure 3.22: Cole-Cole plot when de-ionized water on the cellulose pad

The impedance modulus bode plot on Figure 3.20 has 3 distinct parts: 2 negative slopes interrupted by a flat region. The phase plot on Figure 3.21 shows that

the impedance phase start close to $\theta_z = -90°$, which corresponds to completely capacitive behaviour. It then turns to almost pure resistive impedance ($\theta_z \approx 0°$), and then gets back to capacitive trend. It matches with information on the modulus bode plot. About the Cole-Cole plot on Figure 3.22, the first part is a semi-circle which represent a R-C parallel dipole as explained in section 3.2.1, while the second part is a vertical line for a purely capacitive behaviour.

3.5.2 Interpretation

The Cole-Cole plot and the Bode plot on Figures 3.22, 3.20 and 3.21 validate the equivalent electrical circuit presented in section 3.1 and reproduced on Figure 3.23.

As explained on section 3.1, a semi-circle on the Cole-Cole plot represents a R-C parallel dipole while a vertical line corresponds to a capacitance. Having both behaviours on the same graph can be thus interpreted as a capacitance in series with a R-C parallel dipole. Since the dipole occurs at larger frequencies, we can deduce that the serial capacitance C_{ins} is larger than the one in the dipole C_{sol}. Whenever the frequency is too small to let current pass through the serial resistance, the circuit behaviour is strictly capacitive. As soon as the serial capacitance can be considered as a short circuit, the behaviour linked to R-C parallel dipole appears. This can be matched to the electrical equivalent circuit as presented on Figure 3.23.

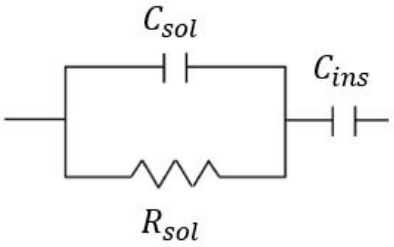

Figure 3.23: Equivalent electrical circuit of the sensor

The bode plot of impedance modulus $|Z_{IDE}|$ behaves as expected, following the behaviour of Figure 3.2. The 2 cut-off frequencies (3.12) and (3.13) clearly appear on the graph. The first negative slope in Figure 3.20 thus corresponds to C_{ins} predominance, the flat part represents the solution resistance R_{sol}, and the

second negative slope is linked to C_{sol} value.

$$f_z = \frac{1}{2\pi R_{sol}(C_{sol} + C_{ins})} \tag{3.12}$$

$$f_p = \frac{1}{2\pi R_{sol} C_{sol}} \tag{3.13}$$

3.6 Changes in hydration level

Using the assembly of Figure 2.14, another test is run to observe the impedance evolution with regard to the hydration level. The same inputs ($50mV$ AC potential, $[1kHZ - 1MHz]$ frequency range) are applied to the sensor.

Using a lab dropper, the solution concentration is controlled. The tested volumes are: $5\mu L, 10\mu L, 20\mu L, 40\mu L, 60\mu L$ and $80\mu L$. After $80\mu L$, the measurement is no longer interesting because the cellulose pad is water-saturated.

After each measurement, the cellulose pad is changed to avoid alterations due to liquid evaporation that can occur for really small volumes, since the measurement (frequency sweep analysis) already takes 2 minutes and a half. The test has been realized twice, once with de-ionized water, and another time with a fixed salt concentration: 100mM.

3.6.1 Results

On Figures 3.24 and 3.25, the impedance modulus and phase of the different volumes of de-ionized solution are shown. On the modulus plot, we can easily discriminate between the three smaller volumes, but the larger ones are less easy to separate. However, on the phase plot, we can see that the plots are shifted over laterally, with decreasing volumes. The $5\mu L$ plot does not behave as the others, and follow a purely capacitive behaviour.

Figures 3.26 and 3.27 represent the test with $100mM$ NaCl solution. It appears that both $5\mu L$ and $10\mu L$ plots behave as capacitive. The discrimination between curves is even harder, if not impossible. On the phase plot, the lateral shift of the maximum does not occur.

The graphs on Figures 3.28 and 3.29 reflect the components values obtained by fitting for both batteries of tests.

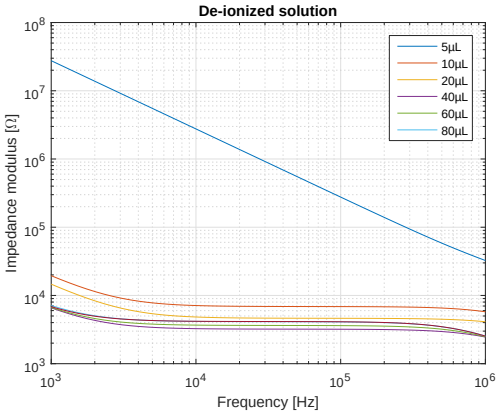

Figure 3.24: Comparison of impedance modulus for different volumes of de-ionized water

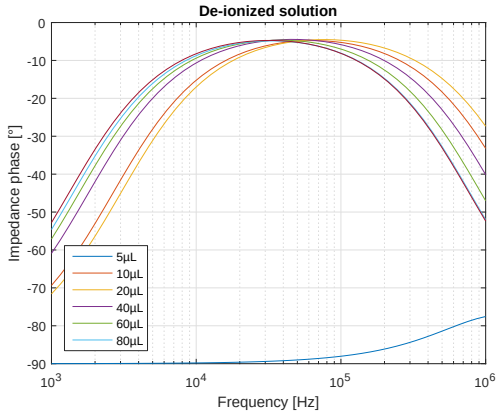

Figure 3.25: Comparison of impedance phase for different volumes of de-ionized water

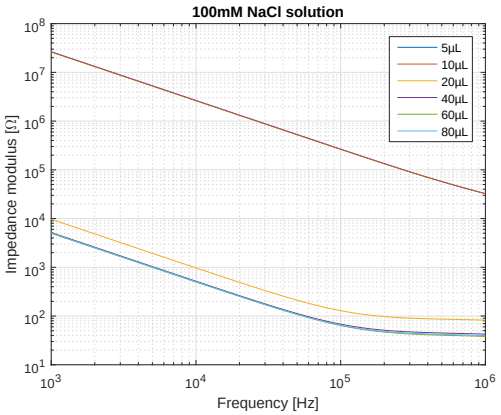

Figure 3.26: Comparison of impedance modulus for volumes of 100mM NaCl solution

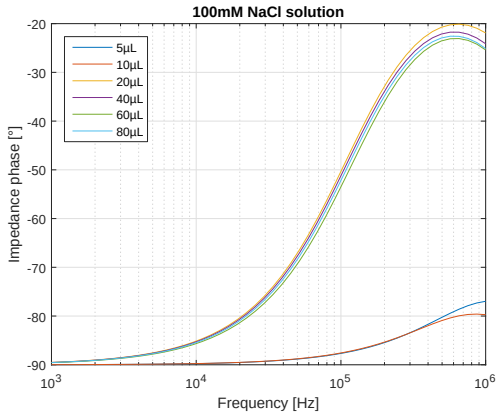

Figure 3.27: Comparison of impedance phase for volumes of 100mM NaCl solution

3.6.2 Interpretation

The $5\mu L$ de-ionized solution curve and the $5\mu L$ and $10\mu L$ 100mM NaCl solution curves behave as purely capacitive. For the de-ionized water, the water is sensed but the amount is so small that the resistance stay high, resulting in only capacitive behaviour. For the saline water, the solution is simply not detected by the sensor. We can prove it by looking into the component values in Table B.2: the insulating capacitance is smaller than the solution capacitance, meaning that as soon as the frequency becomes high enough to let current passing through C_{ins}, C_{sol} is already considered as a short-circuit. There is therefore no R-C parallel dipole, so no sensed

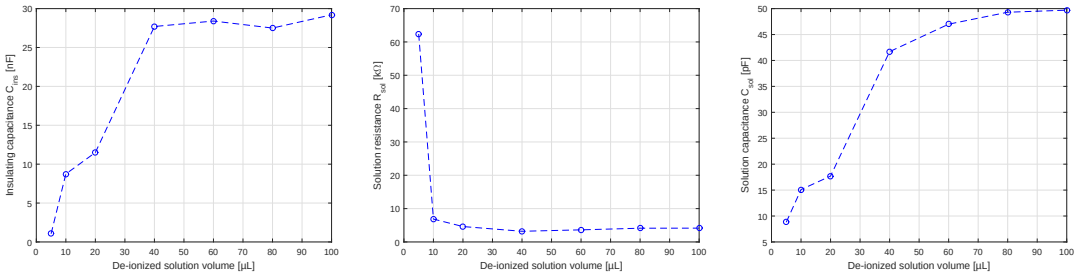

(a) C_{ins} evolution with increasing volume of DI water

(b) R_{sol} evolution with increasing volume of DI water

(c) C_{sol} evolution with increasing volume of DI water

Figure 3.28: Evolution of component values obtained by fitting for different volumes of DI water, based on Table B.2

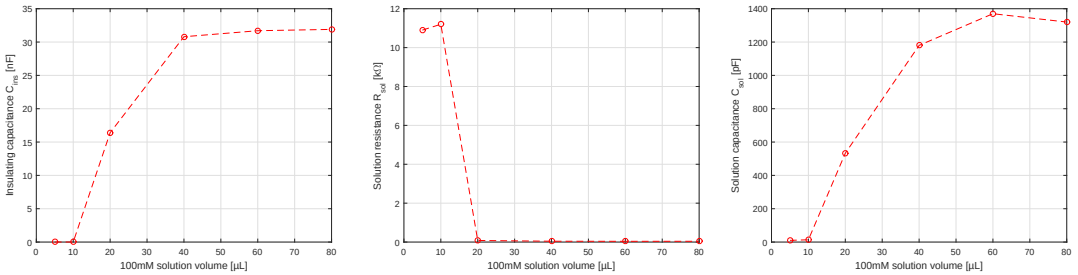

(a) C_{ins} evolution with increasing volume of 100mM NaCl solution

(b) R_{sol} evolution with increasing volume of 100mM NaCl solution

(c) C_{sol} evolution with increasing volume of 100mM NaCl solution

Figure 3.29: Evolution of components values obtained by fitting for different volumes of 100mM NaCl solution, based on Table B.2

solution. In general, for amounts less than $20\mu L$, the detection is not repeatable, both for de-ionized and saline water.

An attractive observation is that for both cases, all curves found themselves within the intervals defined during the first test. On Figure 3.24, the flat zone is comprised between $10^3\Omega$ and $10^4\Omega$, like the curve for DI water on Figure 3.17. The phase maximum values on Figure 3.25 are found between $0°$ and $-10°$, exactly as the maximum phase value on Figure 3.18. This repeatability is also observed for 100mM NaCl solution, where the flat regions of $|Z_{IDE}|$ stands between $10^1\Omega$ and $10^2\Omega$, and the phase maximum values reach the [-20° : -30°] interval, as expected from Figures 3.17 and 3.18. This observation proves the robustness of the first discrimination, since it does not depend on the solution volume, once the water on

the pad is detected.

As explained in the previous section, the maximum phase value depends on the solution resistance value. The higher the resistance, the higher the maximum. But on Figure 3.25, it appears that the phase is also subject to a lateral shift with decreasing volumes. This shift can be explained using the solution capacitance C_{sol}.
As soon as the water is in contact with the whole absorbent pad, allowing all the electrical lines to pass through a liquid material instead of a solid cellulose material, the solution resistance R_{sol} stabilizes for a defined salt concentration, as observed on plots 3.28b and 3.29b. This stabilization happens between $20\mu L$ and $40\mu L$. If the first cut-off frequency might still depend on C_{ins} behaviour, the second cut-off frequency will however only depend on C_{sol} evolution.

While taking a deeper look into Figure 3.25, we can see that the plot is shifted in the minus x-direction with increasing volumes. Since the expression of the second cut-off frequency is $f_p = \frac{1}{2\pi R_{sol} C_{sol}}$ and since R_{sol} is more or less constant, having a decreasing f_p leads to an increasing C_{sol} value. This matches the theory explaining that the relative permittivity of a solution $\varepsilon_{r,sol}$ will increase with volume because of the increasing number of water molecules, and therefore the increasing density of dipoles. To summarize, $\varepsilon_{r,sol}$ and C_{sol} increase with hydration level, shifting the phase plot in the minus x-direction because of the cut-off frequency expression.
On the Bode plot of modulus (Figure 3.24), the only visible information is the solution resistance. On both $10\mu L$ and $20\mu L$ curves, the water is not found on the whole pad surface, the solution resistance therefore decreases with increasing volumes. As soon as the water covers the whole surface, the curves start to be really close to each other since R_{sol} stabilizes, and no further discrimination is possible using this graph. The evolution of R_{sol} follows the theory saying that the conductivity increases with volume because of additional ionic pathways for charge transport.

Concerning the 2 graphs on Figure 3.26 and 3.27 about saline water, the results are not as conclusive as the ones for de-ionized water. The behaviour linked to the solution resistance R_{sol} nevertheless remains, both for $|Z_{IDE}|$ and θ_z. By contrast, the impact of C_{sol} of the plots is not visible. This is more than probably due to the fact that the measurement device is not able to correctly sense the capacitance solution because of the too low frequency range (device limitation to $1MHz$).

3.7 Impact of skin on electrical connections

To completely validate the sensor, a last test is used to see if the sensor placement on the skin will impact the measurement. The sensor will indeed be held in place folded around the thumb. And since it is designed to monitor the everyday life of patients, it will be subject to motion artefacts when the patient uses its thumb.
The folding, the exposure to movement and the contact with the skin are three important steps to validate in order to have a reliable sensor.

3.7.1 Results

To observe the impact of the skin in contact with the routes of the sensor on the tare impedance, two tests are runned: one with direct contact, and the other one using a polyimide sheet between routes and skin to ensure insulation. The sensing unit is still exposed to skin, otherwise the sensing of sweat will be no more possible. Ideally, the ALD layer deposited on the routes shall be sufficient to neglect skin impact.

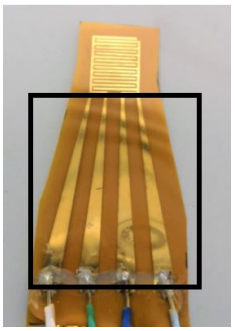

Figure 3.30: Connection routes

As the test is about the tare impedance, no solution at all is present, and the fit is done using a $R_p - C_p$ parallel dipole. If no DC path is created, the R_p will be really high, while the tare capacitance C_p will be around $5 - 6pF$.

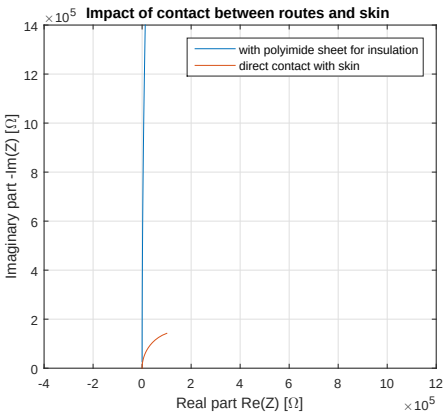

Figure 3.31: Cole-Cole plot of tare capacitance with and without additional insulation

	R_p	C_p
With extra PI sheet	$154M\Omega$	$6.06pF$
Without extra PI sheet	$302k\Omega$	$746pF$

Table 3.3: Components values obtained by fitting for measurement with and without additional insulation

We can observe on the Cole-Cole plot a drastic reduction of the imaginary part value in case of direct contact with skin, confirmed by the related increase in C_p values. The parallel resistance value R_p also decreases, but stays however important.

3.7.2 Interpretation

The impact of the contact between the sensor routes and the skin is not negligible. When adding an extra insulating sheet, the capacitance value match the one of tare capacitance, situated around $5 - 6pF$. But when only the Al_2O_3 passivation layer is present, the capacitance value raises up to $700pF$, which is completely out of range and will distort the results. The resistive value R_p also drastically decreases in case of direct skin contact, which means that there might be a DC path between the routes, short-cutting the measurement of the IDE structure. Therefore, the additional insulating layer is absolutely required to keep sensor behaviours as expected.

Chapter 4

Discussion & perspectives

This section will first discuss the issues encountered both in the design and fabrication part as well as in the experimental validation part, and then suggests further steps to lead towards a complete and viable monitoring sensor that could actually be used in real outside body environment for monitoring of epilepsy.

4.1 Design and fabrication

Concerning the design and fabrication steps, several minor issues were observed, mostly because of the connection routes facing the skin.

- Gold connection routes have been deposited onto polyimide film to bring the connecting pads further away from the sensing unit, and therefore allow easier and proper electrical connections. According to the results in section 3.7, the Al_2O_3 layer is not sufficient for insulating the connection routes from the skin. Repeated friction due to thumb movements might also participate to the removal of this tinny layer. An easy solution to this issue is to cover the connection routes with polyimide, as realized in [22]. The required flexibility properties will be maintained while ensuring efficient and reliable insulation, as shown through our test in section 3.7. Concerning the sensing unit, the additional insulating layer is not needed because the Al_2O_3 is not in direct contact with skin. Also, adding a sheet of polyimide would hinder the attraction of sweat by the absorbent pad, and thus make the measurement impossible.

- To insulate the weld area from the skin, UV epoxy was used. This might not be the optimal solution, because the epoxy becomes quite rigid, removing the flexible characteristics of the sensor. As a first step, one improvement could be to deposit the epoxy more precisely, only on the weld point (see Figure 2.11)

- The length of the connection routes could also be modified to remove discomfort for the patient, and to increase the stability of placement on the skin. For now, the connecting pads are too far away, i.e. on the back of the hand. If, by shortening them, they could stop sooner and end up on the thumb bone, the comfort should be improved as well as the adherence.

4.2 Experimental validation

The first and main issue regarding the sensor validation concerns the evolution of the solution capacitance C_{sol} with increasing salt concentrations. As explained in the experimental validation sections 3.4 and 3.6, the frequency range of the pre-selected measurement device does not allow to fully observe the evolution of the solution capacitance C_{sol}, as well as its impact on the graphs in case of salted solutions. This is due to the increased conductivity value for saline water, leading to a significant decline of R_{sol} value. Because of this reduction, the term $(1+j\omega R_{sol}C_{sol})$ in the expression of Z_{IDE} (3.2) can be estimated as $\approx (1 + j\omega 10^1 \cdot 10^{-12}) \approx 1$ for every value of C_{sol} within its range if the frequency does not strongly increase when compared to typical frequency span in de-ionized water. To be able to properly validate the sensor, an extra measurement device is needed with an bandwidth allowing measurements at a higher frequency range, at least $100MHz$.
Using such a proper measurement device, we should b able to find C_{sol} values for saline water that are smaller than the values of de-ionized water, i.e. $50pF$. As explained in section 2.2.2.1, the relative permittivity of a solution indeed decreases with increasing salt concentrations, because the water molecules get polarized by the Na^+ and Cl^- ions; it thus requires more electric flux to polarize them with regards to the electric field.

Another interrogation concerning the validation step is related to the volume threshold detection. In experiment 3.6, the detection threshold of the sensor is around a volume of $20\mu L$, depending on how the drop falls. It indeed appears that whenever the volume of solution is really small, the liquid might just spread into the cellulose pad, without creating Van der Waals interactions that would ensure proper strong contact between the sensor and the pad. In a certain sense, the pad just continues to float over the sensor when the solution volume is too small. In this case, the sensor does not detect the liquid, and shows a purely capacitive behaviour reflecting the tare capacitance. But when the sensor will be on the thumb in real conditions, held in place by the 3M™Tegaderm™backing layer, pressure will be constantly applied on the sensor, and will hopefully decrease the volume detection threshold, thus leading to more repeatable measurements with smaller volumes. However, the applied pressure might also alter the measurement, and should be tested for complete validation of the sensor.

An important aspect to notice is the correct calibration of the sensor using the cell constant (see section2.2.2.2). The cell constant was firstly defined using a relative permittivity $\varepsilon_{r,sol} = 80$ and a solution capacitance $C_{sol} = 50pF$, and then the geometrical parameters were fixed to get the real cell constant as close

as possible to the estimation. Since using de-ionized water ($\varepsilon_{DI} = 80$), the sensed solution capacitance is around $45pF$, it means that the working principle of the cell constant is quite efficient.

Despite above issues, the results are promising, and might allow identification of both sweat conductivity and permittivity within the same measurement. The conductivity changes materialize as vertical shift in maximum phase value, while the permittivity changes correspond to horizontal shift of the phase. In addition, since the sensor does not need to give absolute values but only relative ones, it does not have to be strongly calibrated, and can be subject to variations between the different measurements. It appears indeed that both the tare capacitance value and the insulating capacitance value were changing depending on the assembly, but still within an acceptable range: $[4 - 6pF]$ for tare capacitance, and $[25 - 35nF]$ for the insulating capacitance. As these values stay constant within the same test battery, they do not affect the measurement, since the sensor is asked to notice changes like tendencies or more abrupt peaks and drops.

4.3 Going further

The work realized in the context of this master thesis is only the first step of a long journey to complete validation of the sensor, in order to claim that it can be used as a tool for detecting and monitoring actual epileptic seizures.

The next step to execute is of course to run the tests using a measurement device than can reach $100MHz$, in order to ensure that C_{sol} of saline water is evolving as expected, and to see if it can also be used as a tool to indicate the volume of saline solution on the pad.

After the completion of the proof of concept part, the following step is to put the sensor in real conditions, by recording sweat generation on the base of the thumb. The sympathetic nervous system can be triggered by deep respiration or stressful situations as exams or horror movies.

Once the sensor is known to work in real conditions, the last step is to record epileptic patients having seizures to see if some systematic patterns in measurement come out, and can reliably be related to either seizure detection or prediction when coupled with other information, like heart rate.

The 2 lists below summarize the remaining steps that have been identified to reach the final objective.

Validation in real conditions

1. Ensure that the pressure applied on the sensor by the Tegardem™bandage does not alter the measurement, but hold the sensor close enough to the skin for reliable sweat detection. The bandage might also alter the measurement by preventing the sweat to evaporate or by preventing the skin to breathe.

2. The pressure, friction and constant presence of sweat might also affect the insulating layer, since it is really thin. To ensure a long lifetime for the sensor, other sustainability tests on the layer robustness should be run.

3. To build a wearable sensor, a chip that will collect data, convert analog signal to digital signal, keep the data in memory and/or transmit these data is needed. There are plenty of embedded chips available on the market, like the MPR121 [40]. Casing and connectics to this chip will also be needed. The four point sensing might not be useful anymore, which will thus reduce the width of the connectics area on the polyimide film. An easy implementation for embedded chip would be to fix it on a sponge wristband.

4. In the tests, only NaCl solutions were tested. However, sweat is a dilute electrolyte solution that contains bicarbonate ($NaHCO_3$), potassium (K^+), NaCl and plenty of other minerals. There is therefore a need to ensure that the sensor still reacts properly to an increase in salt concentration, despite the presence of other minerals. The salt concentration is indeed the more important indicator of sweating rate.

5. For the insulation around the connection routes, the polyimide sheet works perfectly, but the 2 sheets might induce some friction with each other if there are not properly hold together. The easiest solution is to use epoxy to ensure adhesion, but it might also be interesting to spin-coat polyimide on the sheet to be sure that no friction is possible.

6. The external environment has always been neglected in our experiments. The sensor indeed lied on a plastic surface, which diffuses the external electrical field lines. But when placed on the skin, we need to make sure that the 3M™Tegaderm™will fill this role. The sensor must not be subject to external environment variations (room temperature, air humidity, rain, etc).

Detecting patterns linked to epileptic seizures

1. The base of the thumb is part of the palmar surface of the hand, but it is not commonly used in EDA measurement. Using an electrochemical EDA

sensor, some tests should be run to ensure that this zone can effectively be used for emotional sweat detection.

2. The arousal of sympathetic system can be triggered by mental simulation, deep respiration or through stressful situations. Therefore, tests to ensure discrimination between thermoregulation sweating and emotional sweating can be run without actually recording truly epileptic patients.

3. The most complex future step is to observe changes in sweat behaviour that are actually linked to epilepsy. By monitoring epileptic patients with both the new sweat sensor and another reliable way to detect seizures, time-windows corresponding to an on-going seizure shall be high-lighted, and we could thus try to observe some patterns within such time-window for the sake of seizure detection, or beforehand for seizure prediction. By coupling the information collected on the sweat sensor with other existing seizure detection devices, the identification of patterns linked to seizures can be facilitated. Some machine learning will also probably be needed to allow a better seizure detection/prediction and a continuous improvement of the sensor methodology.

Chapter 5

Conclusion

In epilepsy, the need for wearable sensors able to properly and reliably monitor a physiological signal in order to detect seizures is stringent, because one third of epileptic patients suffer from refractory epilepsy. This means that they do not respond to drugs. The epileptic seizures therefore have a great impact on their everyday life, impairing them in many ways, and even sometimes leading them to death. Having a non-invasive wearable sensor able to detect every happening seizure is then the ultimate goal pursued by scientists.

Electrodermal activity is a proven technology for seizure detection which consists in detecting conductance changes on skin due to sweat, when the patient is having a seizure. It happens indeed that some kind of seizures trigger the sympathetic nervous system, which itself activates some specific sweat glands on the glabrous skin. Monitoring the activity of these glands leads to the observation of the arousal of the sympathetic nervous system, which therefore can lead to the detection of seizures.

This master thesis addresses the question of whether some additional sweat parameters could be captured and monitored to enhance seizure detection. Following this path, the work realized in the context of this master thesis is to prove the concept of a sensor able to monitor sweat for epileptic seizure with the ability to observe both conductivity and permittivity changes as additional features.

As a liquid impedance reflects its conductivity and its permittivity, an interdigitated sweat sensor was developed. The interdigitated structure is dimensioned to scan the liquid impedance within an absorbent pad, placed between the sensing unit and the skin, which will attract sweat by capillarity. This sensor is chosen to be flexible so that it can properly fit the skin shape, and to be placed on the glabrous skin of the base of the thumb in order to minimize patient's discomfort and to let the patient execute his/her everyday tasks without being too much disturbed.

The chosen sensor substrate is a polyimide film because of its flexibility. Gold was deposited using Electron Beam Deposition on the substrate for electrode metal, and then covered by an $20nm$ Al_2O_3 insulating layer thanks to Atomic Layer Deposition. This insulating layer is used to insulate the electrodes from the liquid,

and thus to remove liquid-solid interface effects and to allow proper capacitive measurement.

The first test showed that the insulating layer is able to resist flexibility constraints, which was essential in this case. Should that layer have cracked, a DC path would have been created, short-cutting the measurement. Then, using impedance spectroscopy, the equivalent electrical circuit was validated with de-ionized water. The range of sensed solution capacitance C_{sol} completely matches the one defined by the cell constant, a tool used to determine the geometrical parameters of the interdigitated structure.

The two major tests consisted in changing either the salt concentration or the volume of the solution present on the pad, to observe whether any discrimination is possible. The results are really promising concerning the NaCl concentration discrimination. The effect of the solution resistance, which gives information about conductivity, is well observed, and is robust regardless of the hydration level. Regarding the volume changes, the evolution of solution capacitance C_{sol} is clearly visible for de-ionized water, which is also really encouraging. A limitation in validation step has however been encoutered, due to the frequency range of measurements devices available. Because of the limited bandwidth of those devices, the proper observation and characterization of the impedance of saline solution was not possible. Therefore, no conclusion regarding the evolution of C_{sol} with respect to volumes changes could have been drawn for saline water, regardless of the molarity.

However, if results for saline water using proper measurement devices happen to behave like the ones of de-ionized water, the sensor could be used as a 2D discrimination tool for both conductivity changes and permittivity changes.
On the y-direction: When increasing the salt concentration, the solution conductivity σ_{sol} increases, which reduces the solution resistance value R_{sol}. This reduction can be observed on the phase bode plot as a vertical shit : the lower the resistance, the lower the maximum phase value.
On the x-direction: When increasing the volume of solution, the solution permittivity ε_{sol} increases, which raises the solution capacitance value C_{sol}. This rise can be observed on the phase Bode plot as an horizontal shift: the higher the capacitance, the further leftwards is the phase plot.

The impact of both skin contact and placement constraints on the tare capacitance have then been observed, resulting on the assessment that the insulating layer deposited on the connection routes on polyimide are not sufficient to properly insulate the sensor and to prevent skin to have impact on the measurement. But this issue can be rapidly managed using an extra polyimide sheet between connec-

tion routes and skin. That test ended the validation of the sensor to the extent of available measurement devices.

The road to an operable wearable sweat sensor for detecting epilepsy is still long, and starts with a simulation of the sensor in real conditions, i.e. on skin detecting sweat that are generated by the arousal of the sympathetic system. An embedded chip needs to be installed, some additional robustness tests with respect to constant applied pressure or long exposition to water need to be run to ensure a long and stable lifetime to the sensor. After being able to monitor the arousal of the sympathetic nervous system, the detection of sweat patterns linked to epileptic seizures can finally be investigated.

We hope that this master thesis may trigger interesting future research towards an efficient wearable sensor that would improve everyday life of epileptic patients.

Bibliography

[1] K. Vandecasteele, T. D. Cooman, Y. Gu, E. Cleeren, K. Claes, W. V. Paesschen, S. V. Huffel, and B. Hunyadi, "Automated epileptic seizure detection based on wearable ecg and ppg in a hospital environment," *MPDI-Sensors*, 2017.

[2] Y. S. Park, L. R. Hochberg, E. N. Eskandar, S. S. Cash, and W. Truccolo, "Early detection of human focal seizures based on cortical multiunit activity," *Conf Proc IEEE Eng Med Biol Soc*, 2014.

[3] A. Ulate-Campos, F. Coughlin, M. Gainza-Lein, I. S. Fernandez, P. Pearl, and T. Loddenkemper, "Automated seizure detection systems and their effectiveness for each type of seizure," *Elsevier*, 2016.

[4] S. Ramgopal, S. Thome-Souza, M. Jackson, N. E. Kadish, I. S. Fernández, J. Klehm, W. Bosl, C. Reinsberger, S. Schachter, and T. Loddenkemper, "Seizure detection, seizure prediction, and closed-loop warning systems in epilepsy," *Elsevier*, 2014.

[5] K. R. Harreby, C. Sevcencu, and J. J. Struijk, "Ictal and peri-ictal changes in cervical vagus nerve activity associated with cardiac effects," *Medical and Biological Engineering and Computing*, 2011.

[6] A. W. Yuen and J. Sander, "Can natural ways to stimulate the vagus nerve improve seizure control?" *Elsevier*, 2017.

[7] A. F. Al-Bakri, M. F. Villamar, C. Haddix, M. Bensalem-Owen, and S. Sunderam, "Noninvasive seizure prediction using autonomic measurements in patients with refractory epilepsy," *Conf Proc IEEE Eng Med Biol Soc.*, 2018.

[8] M.-Z. Poh, T. Loddenkemper, N. C. Swenson, S. Goyal, J. R. Madsen, and R. W. Picard, "Continuous monitoring of electrodermal activity during epileptic seizures using a wearable sensor," *32nd Annual International Conference of the IEEE EMBS*, 2010.

[9] A. van Westrhenen, T. D. Cooman, R. H. C. Lazeron, S. V. Huffel, and R. D. Thijs, "Ictal autonomic changes as a tool for seizure detection: a systematic review," *Springer, Clinical Autonomic Research*, 2018.

[10] P. Ryvlin, C. Ciumas, I. Wisniewski, and S. Beniczky, "Wearable devices for sudden unexpected death in epilepsy prevention," *Epilespia*, 2018.

[11] H. D. Critchley, "Book review: Electrodermal responses: What happens in the brain," *The Neuroscientist*, 2002.

[12] D. Bovell, "The human eccrine sweat gland: Structure, function and disorders," *Journal of Local and Global Health Science*, 2015.

[13] Skin layers posters. [Online]. Available: https://fineartamerica.com/featured/skin-layers-asklepios-medical-atlas.html?product=poster

[14] M. Asahina, A. Poudel, and S. Hirano, "Sweating on the palm and sole: physiological and clinical relevance," *Springer, Clinical Automonic Research*, 2015.

[15] M.-Z. Poh, N. C. Swenson, and R. W. Picard, "A wearable sensor for unobtrusive, long-term assessment of electrodermal activity," *IEEE Transactions on Biomedical Engineering*, 2010.

[16] V. Dam, M. Zevenbergen, and R. van Schaijk, "Flexible chloride sensor for sweat analysis," *Elsevier - Eurosensors*, 2015.

[17] S. Y. Oh, S. Y. Hong, Y. R. Jeong, H. P. J. Yun, S. W. Jin, G. Lee, J. H. Oh, H. Lee, S.-S. Lee, and J. S. Ha, "Skin-attachable, stretchable electrochemical sweat sensor for glucose and ph detection," *ACS Applied Materials and Interfaces*, 2018.

[18] E. Caberlotto, C. Guillou, L. Colomb, C. Barla, S. Salah, M. Vicic, F. Revol-Cavalier, V. Rat, S. Filipe, and F. Flament, "Developing a new device for continuously recording, in vivo, the excretion rate of sweat (perspiration) in humans," *Wiley*, 2018.

[19] G. Liu, C. Ho, N. Slappey, Z. Zhou, S. Snelgrove, M. Brown, A. Grabinski, X. Guo, Y. Chen, K. Miller, J. Edwards, and T. Kaya, "A wearable conductivity sensor for wireless real-time sweat monitoring," *Elsevier - Sensors and Actuators*, 2016.

[20] S. Yao, A. Myers, A. Malhotra, A. B. F. Lin, J. F. Muth, and Y. Zhu, "A wearable hydration sensor with conformal nanowire electrodes," *Advanced Healthcare Materials*, 2017.

[21] X. Huang, Y. Liu, K. Chen, W.-J. Shin, C.-J. Lu, G.-W. Kong, D. Patnaik, S.-H. Lee, J. F. Cortes, and J. A. Rogers, "Stretchable, wireless sensors and functional substrates for epidermal characterization of sweat," *Strechable Electronics*, 2014.

[22] Y.-Y. Hsu, J. Hoffman, R. Ghaffari, B. Ives, P. Wei, L. Klinker, B. Morey, B. Elolampi, D. Davis, C. Rafferty, and K. Dowling, "Epidermal electronics: Skin sweat patch," *Impact*, 2012.

[23] P. Wei, B. Morey, T. Dyson, N. McMahon, Y.-Y. Hsu, S. Gazman, L. Klinker, B. Ives, K. Dowling, and C. Rafferty, "A conformal sensor for wireless sweat level monitoring," *IEEE Sensors*, 2013.

[24] J.-W. Jeong, M. K. Kim, H. Cheng, W.-H. Yeo, X. Huang, Y. Liu, Y. Zhang, Y. Huang, and J. A. Rogers, "Capacitive epidermal electronics for electrically safe, long-term electrophysiological measurements," *Advanced Healthcare Materials*, 2013.

[25] M. A. Yokus, C. Hass, T. Agcayazi, A. Bozkurt, and M. A. Daniele, "Towards a wearable perspiration sensor," *IEEE Sensors*, 2017.

[26] Capacitors. [Online]. Available: http://www.physics.louisville.edu/cldavis/phys299/notes/elec_capacitors.html

[27] S. Druart, "Designing microsystems for liquid electrical properties and variable magnetic fields measurements," 2013, PhD, UCLouvain.

[28] A. V. Mamishev, K. Sundara-Rajan, F. Yang, Y. Du, and M. Zahn, "Interdigital sensors and transducers," *IEEE*, 2004.

[29] Salt concentration and electrical permittivity of water. [Online]. Available: https://chemistry.stackexchange.com/questions/16434/salt-concentration-and-electrical-permittivity-of-water

[30] Conductivity vs. concentration. [Online]. Available: https://sciencing.com/conductivity-vs-concentration-6603418.html

[31] Conductivity (electrolytic). [Online]. Available: https://en.wikipedia.org/wiki/Conductivity_(electrolytic)

[32] A. V. Mamishev, Y. Du, B. C. Lesieutre, and M. Zahn, "Development and applications of fringing electric field dielectrometry sensors and parameter estimation algorithms," *Journal of Electrostatics*, 2001.

[33] X. Wang, Z. Liu, and T. Zhang, "Flexible sensing electronics for wearable/attachable health monitoring," *Advanced Science News*, 2017.

[34] 3M Science. Applied to life ®. [Online]. Available: https://www.3mbelgique.be/3M/fr_BE/company-base-bnl/all-3m-products/~/

Tous-les-produits-3M/Sant%C3%A9/Secteur-m%C3%A9dical/Soins-cutan%C3%A9s-et-traitement-des-plaies/Pansement-pour-soins-de-plaie/Tegaderm/?N=5002385+8707795+8707798+8711017+8711098+8711132+8711738&rt=r3

[35] Autolab PGSTAT302N. [Online]. Available: https://www.metrohm.com/fr-be/products-overview/electrochemistry/autolab-modular-line/PGSTAT302N

[36] N. Couniot, "Highly-sensitive CMOS capacitive biosensors towards detection of single bacterial cell in electrolyte solutions," 2015, PhD, UCLouvain.

[37] Capacitance measurement. [Online]. Available: https://www.sciencedirect.com/topics/engineering/capacitance-measurement

[38] Boltzmann constant. [Online]. Available: https://en.wikipedia.org/wiki/Boltzmann_constant

[39] Probe system MPI TS3000-SE. [Online]. Available: https://www.mpi-corporation.com/ast/engineering-probe-systems/mpi-automated-systems/ts3000-se-probe-system/

[40] MPR121 12-Key capacitive touch sensor. [Online]. Available: https://learn.adafruit.com/adafruit-mpr121-12-key-capacitive-touch-sensor-breakout-tutorial/overview

Appendix A

State-of-the-art Illustrations

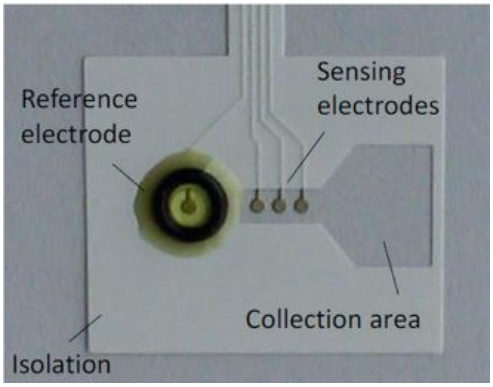

Figure A.1: electrochemical sensing of Cl^- [16]

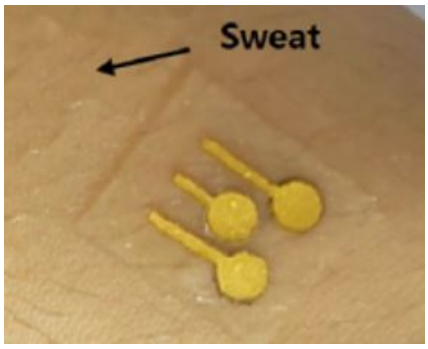

Figure A.2: electrochemical sensing of glucose and pH in sweat [17]

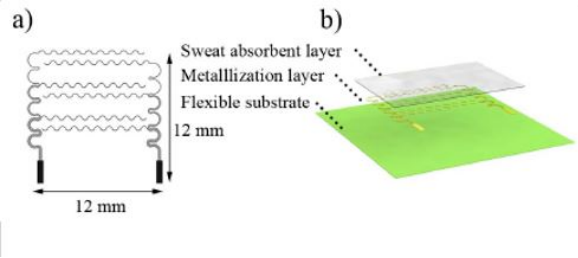

Figure A.3: IDE sensing of conductivity changes due to Na+ and Cl- concentration [25]

Figure A.4: IDE sensing skin hydration level by change of impedance due to increased dielectric constant [20]

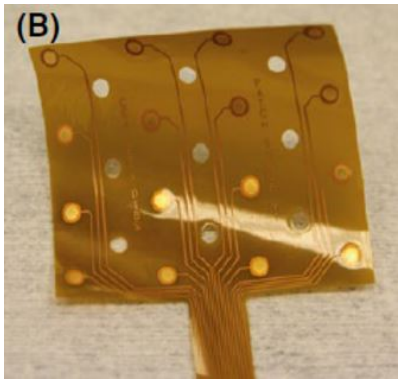

Figure A.5: sensing of increased conductance on armpits [18]

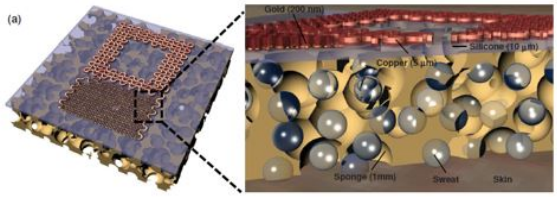

Figure A.6: LC resonators with capacitive electrodes for volume and chemical properties of sweat [21]

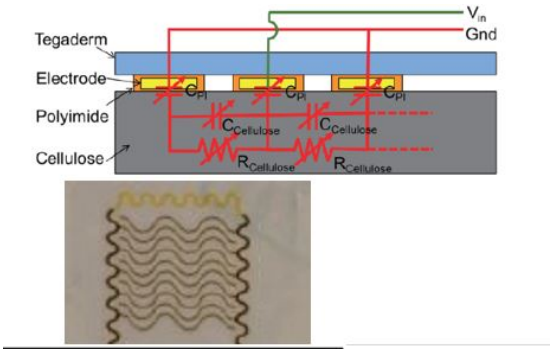

Figure A.7: IDE sensing of skin hydration level through RC measurements [22]

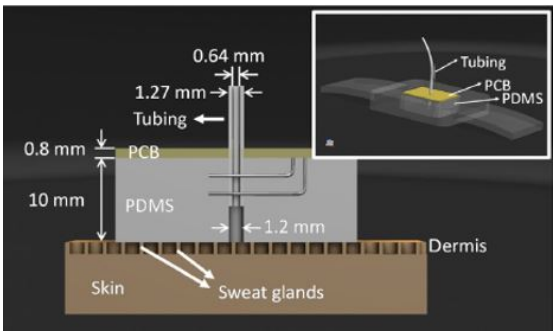

Figure A.8: sensing of conductivity changes with RC parallel dipole [19]

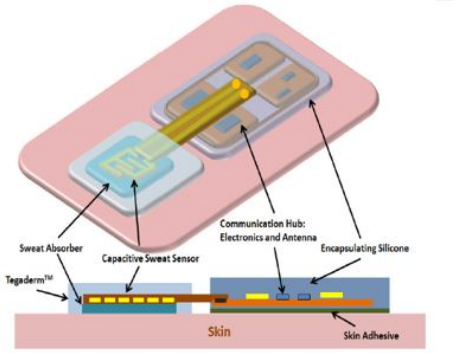

Figure A.9: IDE sensing of sweat rate and level through capacitance [23]

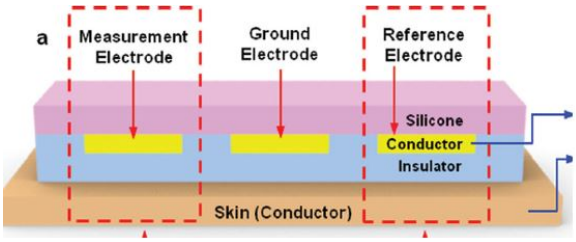

Figure A.10: capacitive coupling through insulating layer [24]

Appendix B

Experiments results

B.1 Flexural strength of insulating layer 3.2

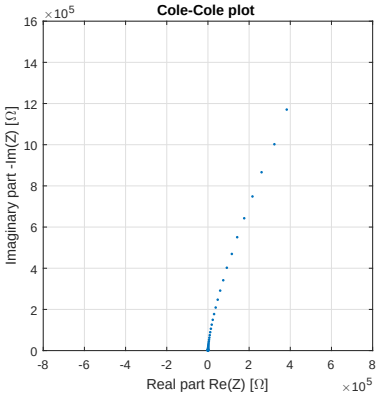

(a) Test №2: Cole-Cole plot

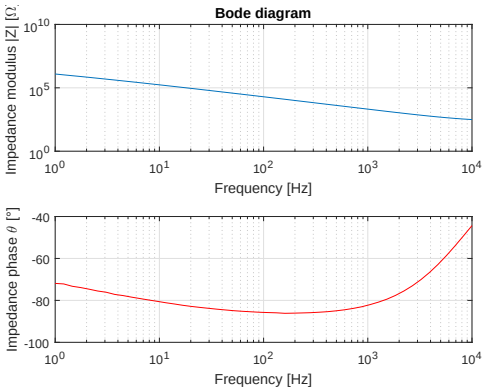

(b) Test №2: Bode plot

Figure B.1: Test №2: DUT folded around a 4cm diameter tube

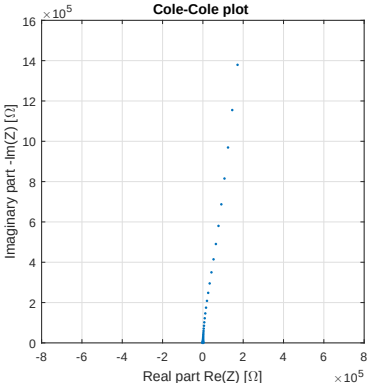

(a) Test №3: Cole-Cole plot

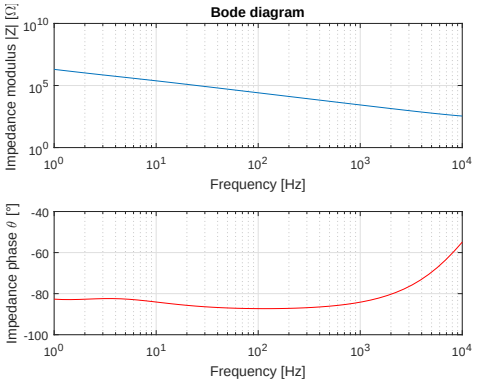

(b) Test №3: Bode plot

Figure B.2: Test №3: DUT folded around a 3.2cm diameter tube

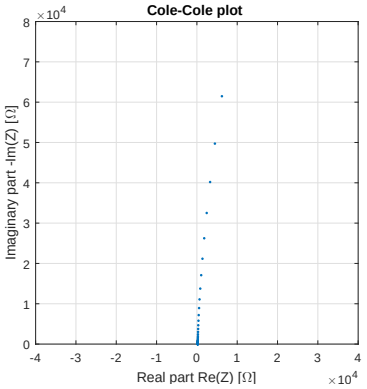

(a) Test №4: Cole-Cole plot

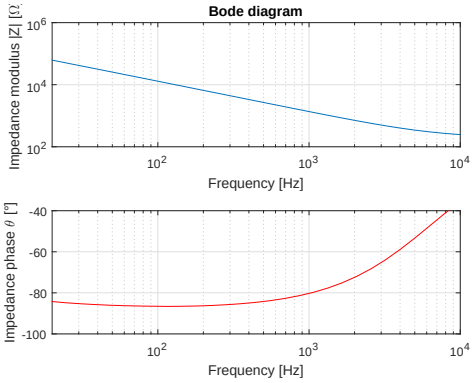

(b) Test №4: Bode plot

Figure B.3: Test №4: DUT folded around a 1.6cm diameter tube

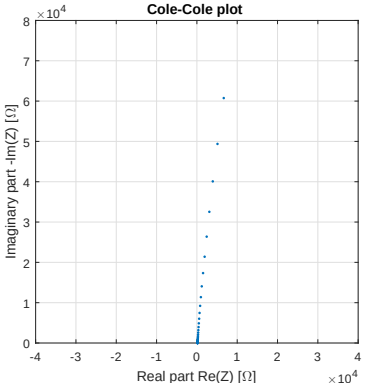

(a) Test №5: Cole-Cole plot

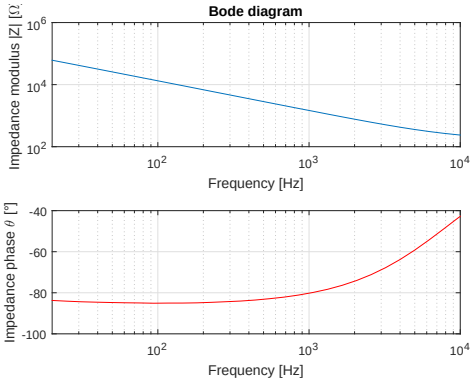

(b) Test №5: Bode plot

Figure B.4: Test №5: DUT folded around a 1.2cm diameter tube

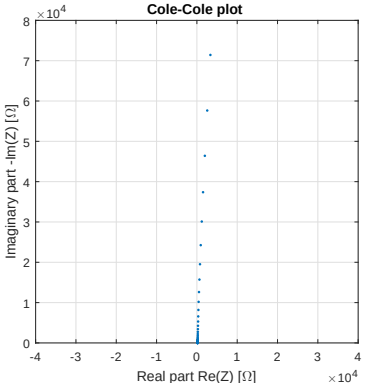

(a) Test №6: Cole-Cole plot

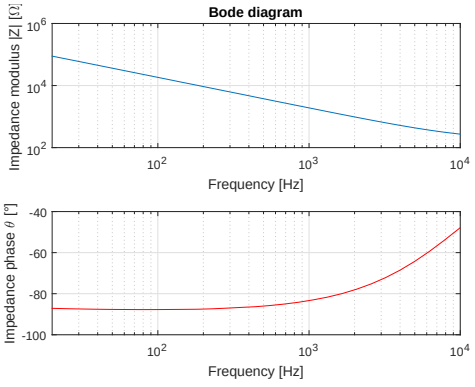

(b) Test №6: Bode plot

Figure B.5: Test №6: DUT folded around a 1cm diameter tube

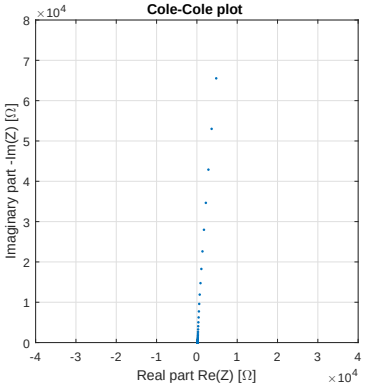

(a) Test №7: Cole-Cole plot

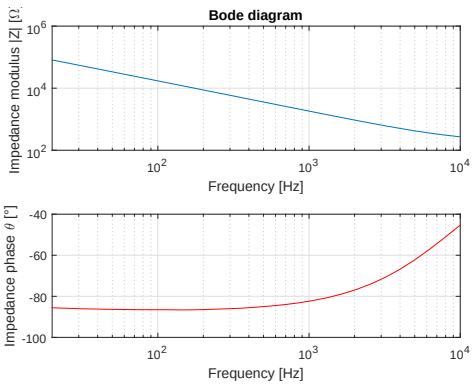

(b) Test №7: Bode plot

Figure B.6: Test №7: DUT folded around a 0.8cm diameter tube

B.2 Changes in salt concentration 3.4

[NaCl][M]	C_{ins} [F]	R_{sol} [Ω]	C_{sol} [F]
DI	29.4n	2.94k	44.6p
DI	26.5n	1.76k	44.7p
DI	26n	2.03k	48.7p
DI	26.8n	1.48k	40.3p
10m	33.7n	76.3	551p
10m	33.9n	77.4	540p
10m	30.3n	90.4	453p
50m	34.2n	55.1	697p
50m	34.3n	55.9	763p
50m	34.1n	53	822p
50m	32.8n	52.7	760p
50m	32.9n	53.2	817p
100m	35.1n	42.9	1.02n
100m	33.3n	41.5	1.1n
100m	34.2n	38.5	1.11n

Table B.1: Components values obtained by fitting in salt concentration changes test

B.3 Changes in hydration level 3.6

Concentration	Volume	C_{ins}	R_{sol}	C_{sol}
DI water	$5\mu L$	$1.05nF$	$62.4k\Omega$	$8.81pF$
	$10\mu L$	$8.74nF$	$6.86k\Omega$	$15.1pF$
	$20\mu L$	$11.5nF$	$4.62k\Omega$	$17.7pF$
	$40\mu L$	$27.7nF$	$3.2k\Omega$	$41.7pF$
	$60\mu L$	$28.4nF$	$3.63k\Omega$	$47pF$
	$80\mu L$	$27.5nF$	$4.12k\Omega$	$49.3pF$
	$100\mu L$	$29.2nF$	$4.14k\Omega$	$49.7pF$
100mM solution	$5\mu L$	$6pF$	$10.9k\Omega$	$10.2pF$
	$10\mu L$	$6.08pF$	$11.2k\Omega$	$13.8pF$
	$20\mu L$	$16.4nF$	82.3Ω	$533pF$
	$40\mu L$	$30.8nF$	42.6Ω	$1.18nF$
	$60\mu L$	$31.7nF$	38.1Ω	$1.37nF$
	$80\mu L$	$31.9nF$	39.8Ω	$1.32nF$

Table B.2: Components values obtained by fitting for different volumes of solution

UNIVERSITÉ CATHOLIQUE DE LOUVAIN
École polytechnique de Louvain
Rue Archimède, 1 bte L6.11.01, 1348 Louvain-la-Neuve, Belgique | **www.uclouvain.be/epl**